atmosphere

MDPI

Review

The Widespread Use of Remote Sensing in Asbestos, Vegetation, Oil and Gas, and Geology Applications

Leydy K. Torres Gil, David Valdelamar Martínez and Manuel Saba *

Civil Engineering Program, Universidad de Cartagena, Cartagena 130001, Colombia
* Correspondence: msaba@unicartagena.edu.co

Abstract: Remote sensing is the technique of acquiring data from the earth's surface from sensors installed on satellites or on manned or unmanned aircrafts. Its use is common in dozens of sectors of science and technology, agriculture, atmosphere, soil, water, land surface, oceans and coasts, snow and ice, and natural disasters, among others. This article focuses on an in-depth literature review of some of the most common and promising disciplines, which are asbestos–cement roof identification, vegetation identification, the oil and gas industry, and geology, with the aim of having clarity on the trends in research on these issues at the international level. The most relevant problems in each sector have been highlighted, evidencing the need for future research in the area in light of technological advances in multi- and hyperspectral sensors and the availability of satellite images with more precise spatial resolution. A bibliometric analysis is proposed for each discipline and the network of related keywords is discussed. Finally, the results suggest that policymakers, urban planners, mine, and oil and gas companies should consider remote sensing as primary tool when planning comprehensive development strategies and in field parameter multitemporal analysis.

Keywords: remote sensing review; vegetation index; oil spill detection; soil identification

Citation: Torres Gil, L.K.; Valdelamar Martínez, D.; Saba, M. The Widespread Use of Remote Sensing in Asbestos, Vegetation, Oil and Gas, and Geology Applications. *Atmosphere* **2023**, *14*, 172. https://doi.org/10.3390/atmos14010172

Academic Editor: Filomena Romano

Received: 13 December 2022
Revised: 3 January 2023
Accepted: 9 January 2023
Published: 13 January 2023

1. Introduction

Remote sensing is the process of detecting and monitoring the physical characteristics of an area by measuring its reflected and emitted radiation at a distance [1–5]. Electromagnetic (EM) energy, produced by the vibration of charged particles, travels as waves through the atmosphere and the vacuum of space [6–8]. These waves have different wavelengths (the distance from wave crest to wave crest) and frequencies; a shorter wavelength means a higher frequency. Some waves, such as radio, micro-, and infrared waves, have longer wavelengths, while others, such as ultraviolet rays, X-rays, and gamma rays, have much shorter wavelengths. Visible light is in the middle of that range of long- to short-wave radiation. This small portion of energy is all that the human eye is capable of detecting. Instrumentation is needed to detect all other forms of electromagnetic energy (see Figure 1 taken from [2]).

Some waves are absorbed or reflected by atmospheric components, such as water vapor and carbon dioxide, while some wavelengths allow unimpeded movement through the atmosphere; visible light has wavelengths that can be transmitted through the atmosphere. Microwave energy has wavelengths that can pass through clouds, an attribute used by many weather and 5rftcommunication satellites. All things on earth reflect, absorb, or transmit energy, the amount of which varies by wavelength, creating a spectral fingerprint, called a spectral signature, unique to each object [9]. Remote sensing sensors sense the EM waves reflected/emitted by the objects on the Earth's surface. The sensors record these waves as images depending on their spectral capabilities.

Spectral sensors collect remote sensing images taken via drone, plane, or satellite. They can be used in the environmental field to monitor changes in temperature in the land surface, oceans and in the topography of the ocean floor [10,11], map great forest

fires [12–14], track clouds to help predict the weather [15,16], or observe volcanoes erupt and help monitor dust storms [17,18]. Additionally, among its most common applications are the monitoring of the growth of a city through multitemporal analysis [19,20], the identification of objects on the ground, military, intelligence, commercial, planning, and humanitarian applications, among others [21].

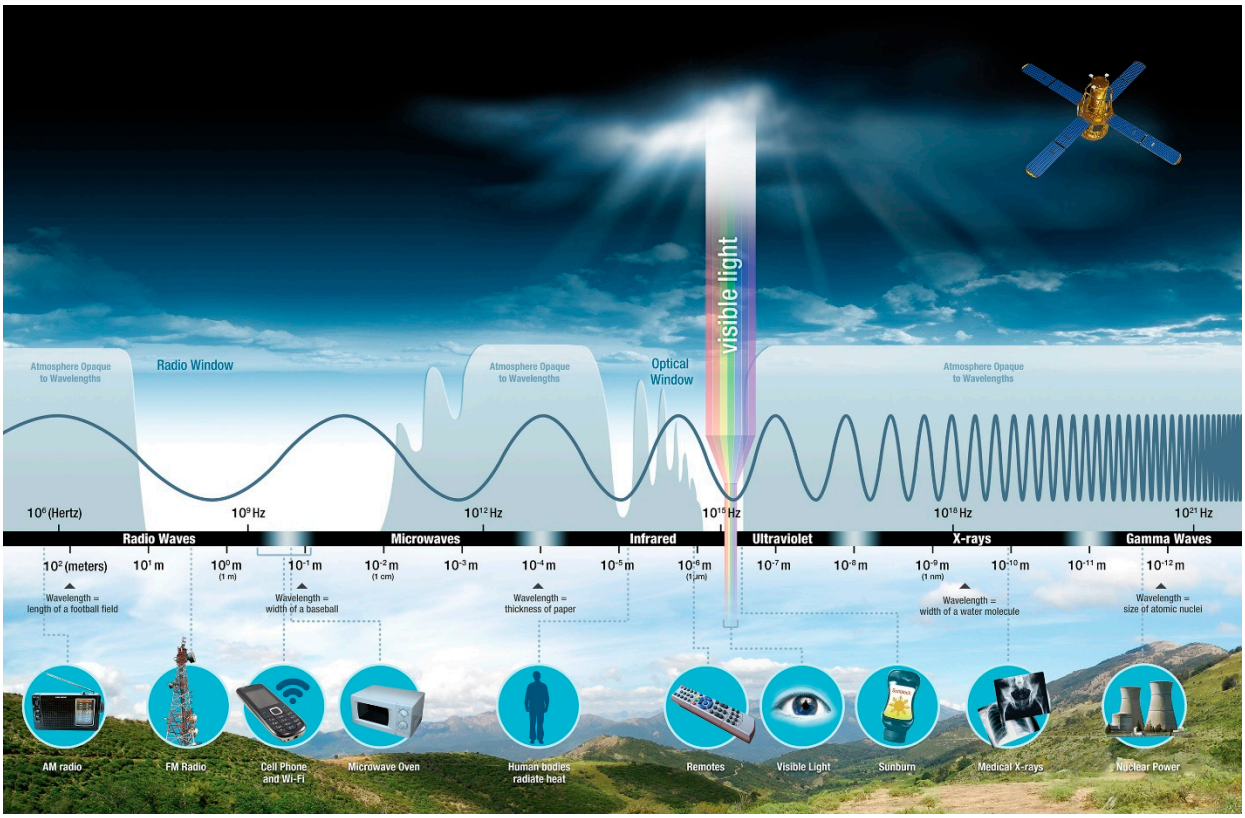

Figure 1. Diagram of the electromagnetic spectrum. Source: NASA Science [2].

As remote technologies continue to develop, their use is becoming more widespread and multidisciplinary [22–29]. Often, review works focus mainly on one highly specific topic [22–29], while a comparison between remote sensing applications is neglected.

The present study focuses particularly on the selected applications of remote sensing for civil and environmental engineering, such as the identification of asbestos–cement roofs, vegetation and its health status, oil and gas, and geological applications. The authors acknowledge the fact that many other applications of remote sensing exist and are of primary interest in the academic world; nevertheless, in this work, the topics were narrowed for extension. This review includes the most relevant papers on the matter in the last decades found mainly in Science Direct, Scopus, and SpringerLink databases. A historical cross section of research on the subject aims to detect past and present trends, thinking about possible developments in the coming years.

2. Methodology

The thirty most relevant articles of each topic treated were identified considering the number of citations and the relevance of the journal. They were read in order to be filtered, tabulated, and finally included in the discussion of this document. This review reports a chapter for each main application. Where relevant, the keywords network was analyzed. Finally, an original discussion of the spectral signature is presented, which is useful for the reader while comparing different applications for similar materials to identify a pattern that is useful for future policy makers' decisions and future research.

3. Remote Sensing and Asbestos–Cement Roofs

In the 1940s to 1990s, asbestos was widely used as an additive in construction materials [30–32]. This mineral is formed by a group of fibrous microcrystalline hydrated silicates, among which Chrysotile stands out in the form of serpentines. On the other hand, thermolite, crocidolite, actinolite, anthophyllite, and amosite are classified as part of the amphibole's family. All of them are considered carcinogenic to humans by the International Agency for Cancer Research (IACR) and by the World Health Organization (WHO) [33–35]. The risk of this mineral to humans has been known approximately since the first decades of the 20th century. The danger is mainly due to the inhalation of fibers that, penetrating into the respiratory system, cause permanent damage in humans, producing diseases such as asbestosis, pleural thickening, neoplastic diseases such as lung cancer, mesothelioma of the pleura, and peritoneum, among others [36]. The use of asbestos on a large scale began around World War II, with an annual world production of 1 million metric tons in 1950 up to 5 million in 1975. In 2000, a cumulative world production of approximately 173 millions of tons was estimated [37]. More recently, in 2021, independent agencies estimated that the annual world production of asbestos was still at 1.29 million metric tons [38], mainly in Russia, Kazakhstan, China, and Brazil.

Due to the great impact on public health that occurs due to the inhalation of asbestos fibers, it is vitally important to invest in methodologies that seek to estimate the amount of this mineral in the urban environment, where people are more exposed. This is especially the case for countries that have recently prohibited the use and commercialization of the material, as it would allow the competent authorities to formulate strategies to mitigate the environmental and public health problem.

One of the first steps to mitigate the public health problem [37,39–42] is the identification of the distribution of asbestos–cement roofs through remote sensing from spectral images. As evidenced in the literature [30,43,44], for the capture of this type of image, multispectral sensors are particularly used, with a band range between 400 nm and 2400 nm. The sensor can be mounted on an unmanned aircraft (drone), on a manned aircraft, and on satellites.

The relationship between the spatial resolution (SRE) and the economic factor is one of the most relevant factors when choosing between the three modalities mentioned above. The unmanned aircraft guarantees the SRE of the order of centimeters, with a flight height between 100 m and 300 m [45,46]. However, when it comes to identifying large areas, such as cities or entire regions, this tool has strong logistical limitations; companies providing this service are scarce and the costs are very high. On the other hand, the overflight with a manned aircraft could reach an SRE between 0.4 m and 2.0 m with a flight height between 500 m and 1500 m. The relationship between the SRE and cost is acceptable, although it costs between 600 and 1000 USD per km^2, which makes it a common tool in developed countries and scarcely used in developing countries such as those in South America [47]. The third option, through satellite images, has been highly debated in the international scientific community in recent years. This is because until 2020, the SRE of WorldView-3 images had 7.5 m pixels (56.25 m^2) for eight short-wave infrared (SWIR) bands [48]. Considering that most roofs have a dimension equal to or less than 56.25 m^2, this method is not effective according to the literature [44,49]. However, to date, thanks to technological advances, the satellite images that are on the market offer an SRE of 3.70 m (13.69 m^2) in the SWIR band range between 1000 nm and 2400 nm [50], and an SRE of 0.30 m (0.09 m^2) in the band range between 400 nm and 1000 nm (eight bands in the visible and near-infrared (VNIR) region). This makes them attractive since they have limited costs and do not require flight permits or particular logistics to purchase them directly from official suppliers.

In the last two decades, the use of remote sensing has proven to be a good instrument to identify and evaluate the condition and material of roofs [30,51,52] (Table A1). There are different methodologies for classifying asbestos–cement roofs through the use of multispectral and hyperspectral images, which focus on algorithms such as object classification or object-based image analysis (OBIA) [53], Spectral Feature Fitting (SFF) [54], Spectral Angle

Mapper (SAM) [43], Support Vector Machine (SVM) [55], decision trees and Random Forest (RF), discriminant function analysis (DFA) [56], and the maximum likelihood method (MLC), among others. The use of Convolutional Neural Networks (CNNs) has also been implemented [44] for the identification of asbestos–cement tiles with the use of aerial RGB and color–infrared (CIR) imagery.

OBIA is characterized by simulating the way in which human beings perceive and recognize objects in the real world. The analysis begins by segmenting an image into homogeneous regions or objects that roughly represent real-world objects. This approach is based on the idea that the information in an image should be interpreted as significant objects rather than individual pixels, classified from spectral, spatial, textual, and contextual data [53]. On the other hand, the SFF classification method is responsible for comparing the image pixel spectrum with a reference spectrum from a spectral library or a field/laboratory spectrum. [54]. Something similar is conducted by the SAM and SVM algorithms. In the case of SAM, this allows one to quickly map the similarities between the image spectra and the reference spectra by calculating the angle formed between the spectra. This algorithm is used in the ENVI® software [57]. Similarly, the SVM is a supervised machine learning statistical algorithm that analyzes the data and recognizes patterns based on a decision plane that defines the decision boundary that separates objects with different class memberships [53]. On the other side, RF is a machine learning algorithm that works based on the bagging method and the classification and regression tree, in which each tree contributes a single vote to determine the most frequent class in a set of variables data [58,59].

In attempts to identify asbestos–cement roofs, the trend is to increase the overall accuracy of the classification by reducing the error of the algorithm through the delimitation of the construction areas. Abriha et al. (2018) [56] carried out the identification of asbestos–cement tiles in the city of Debrecen in Hungary through a mask with the normalized digital surface model derived from a Digital Terrain Model and a digital surface model using a LiDAR study, in addition to another mask with the values obtained from the Normalized Difference Vegetation Index (NDVI). At the time of classification, the discrimination of tiles was made by those that were shaded and sunny. However, the classification accuracy was 6–7 percent worse compared to the simple approach that did not discriminate, so it is not particularly efficient to perform this procedure.

In another study carried out in the same city mentioned above by Szabó et al. (2014) [51], the same procedure was carried out for the delimitation of the construction areas without including the LiDAR model, giving a global precision of almost 80% against 85% where the model was applied. On the other hand, it was shown that the DFA and RF classification methods that were applied by [56] showed better results compared to SVM, SAM, and MLC [51].

Tommasini et al. (2019) [30] filtered areas in image that were not covered by buildings using a vector mask with a layer of cadastral forms. This involved a topographic map where all the buildings related to the selected area were described using a vector graphics editor. The clipping operation was performed using functions offered by the free software QGIS. Something similar was performed in the study carried out by Cilia et al. (2015) [52] in five municipalities located in northern Italy, where the cadastre map was superimposed on a multispectral infrared visible imaging spectrometer (MIVIS) to improve the classification. In addition, roofs with surfaces less than 36 m^2 were excluded due to the 3 × 3 m resolution of the images. However, Frassy et al. (2014) [43] established that MIVIS data from the Valle d'Aosta region, Italy, with a spatial resolution of 4 × 4 m, assume that at least a 3 × 3 pixel window containing asbestos–cement roofing is needed for correct detection to occur, classifying roofs larger than 144 m^2 with reasonable confidence. These assumptions can influence the accuracy of the classification. The authors found a 43% correct classification independent of the roofs size and 75% when only roofs bigger than 3 × 3 pixels were considered. Krówczyńska et al. (2016) [44] found similar results with an accuracy of 60% for surfaces up to 300 m^2 and 20% for roof surfaces smaller than

3 × 3 pixels. On the contrary, Cilia et al. (2015) [52] obtained better results by applying the same algorithm with precisions of 86% and 89%, respectively, showing the impact of spatial resolution when making the classification. Hence, the finer the spatial resolution, the better the performance of the classification algorithms.

Methodologies to improve spatial resolution are available, such as pansharpening, which is an improvement in the geometric resolution of multispectral bands with the finer resolution of the panchromatic band. This method tends to affect the spectral profiles of the objects; nevertheless, it improves the spatial characteristics. This method is applied when a pixel is larger than a possible house, so its values are mixed with those of the environment, making the spectral profiles not accurate. Pansharpening has been used in different works found in the literature, such as Abriha et al. (2018) [56], where this technique improved the classification by 2–3%. It was also used in the cities of Kajang and Bangi, Malaysia, for the determination of asbestos–cement tiles in buildings, achieving an accuracy of up to 93.10%, [53].

These methods from hyperspectral and multispectral images present in some cases low resolutions or little information within the spectral range. To ensure that they cover a spectral range and a high spatial resolution, the costs increase significantly. For this reason, over time, other methodologies have been studied that have high spatial resolutions, do not need spectral information, and are cheaper. Among these is the use of CNNs, which were introduced theoretically for the first time by LeCun et al. (1989) [60]. However, the first practical use was probably by Krizhevsky in 2012 [61]. The network was named AlexNet and was used to classify images from the ImageNet library. Neural networks are characterized by having greater precision than other methods used. Nevertheless, to classify asbestos–cement tiles, it was used for the first time by Krówczyńska et al. (2020) [44] in Checiny, Polonia. RGB and color–infrared (CIR) images were used and global accuracies of 89% were obtained. According to the authors, this could be a more economical and practical method for the identification of both roof types and other areas of interest.

Remote sensing has been widely studied worldwide, mainly for the identification of vegetation, minerals, and oil spills. However, in the case of asbestos–cement tiles, studies are still limited in the literature. The first part of Table A1 shows an overview of the most recent and cited works found in the literature in the matter of asbestos identification. A comparison between the classification results in WV3 satellite images (multispectral) and hyperspectral images is not found in the literature. This would allow for an assessment of the technical–economic feasibility of the two options, favoring greater awareness in decision making by authorities and professionals.

The words *Remote sensing* and *Asbestos* were searched for in *Scopus*, resulting in 708 works; then, through the free platform VOSviewer, the network of related keywords and their distribution per year were obtained (Figure 2). It is clear that in general, the issue of the remote sensing of asbestos–cement has had its greatest relevance in the last 20 years, due to strict regulation, especially in European countries [62], which has led to a greater sensitivity in the authorities and the academic world on the subject. The use of the words airborne remote sensing, MIVIS, multispectral infrared marked the 2000s [54], especially in studies in Italy, which also appeared as a keyword; however, in the last 5 years, the most trending keywords have been hyperspectral, machine learning, satellite data, and satellite imagery, showing an evolution in technology towards more precise sensors with higher bands both in aircrafts and at a satellite level [56,63]. The need to have greater spatial resolution and the costs of these images are the two contrasting factors that dominate the academic and professional scene. The dominant countries in these investigations are the United States, Italy, and China; however, adding the studies of European countries, it is noted that this continent represents the true center of research on asbestos and remote sensing worldwide. Asia also plays an important role as China, India, and Malaysia are dominant countries in these investigations, while Latin America has a deep lack of studies.

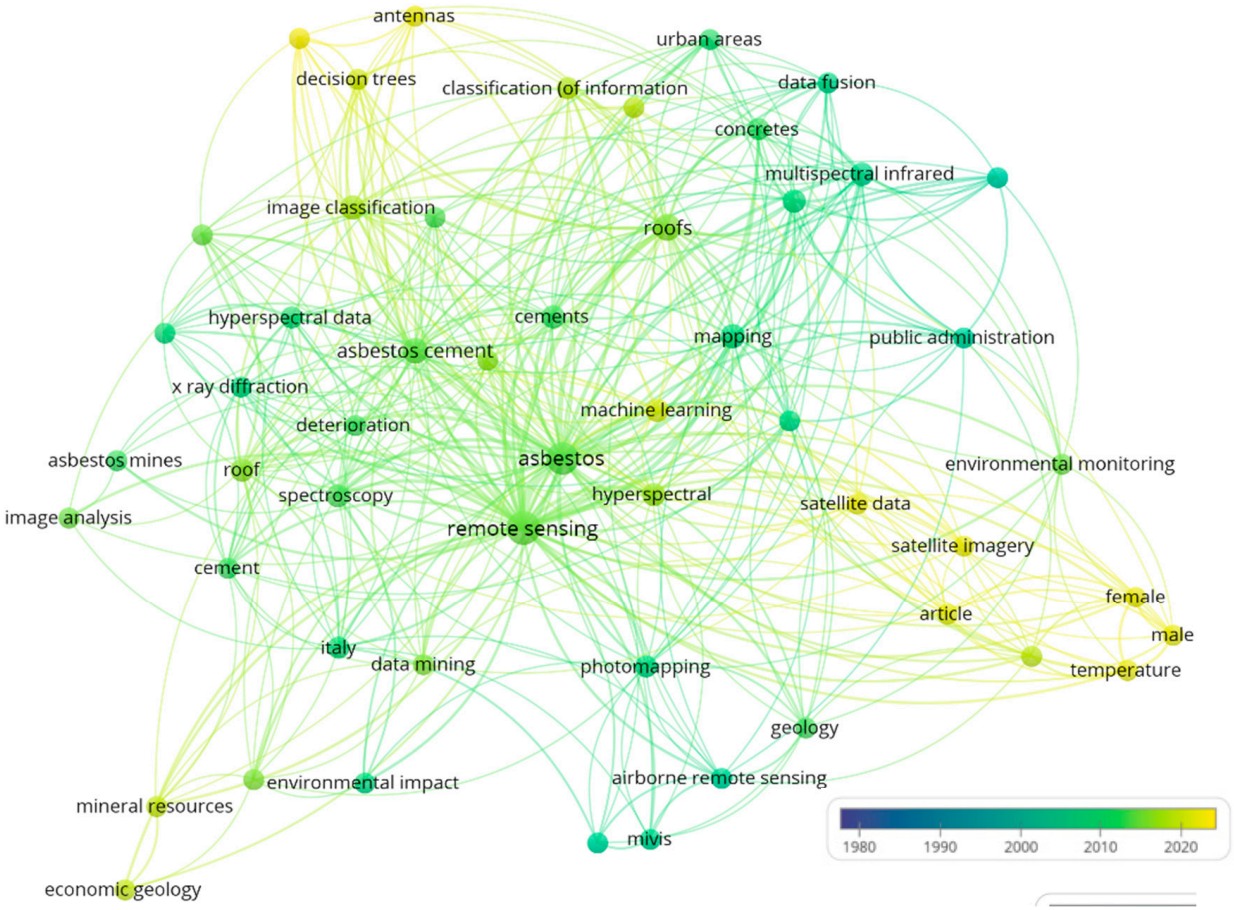

Figure 2. Relationship between keywords found in Scopus per year. Graph made with VOSviewer.

4. Remote Sensing and Vegetation

Vegetation studies are carried out for the planning and management of land use through studies of vegetation cover, the determination of changes caused by fires, the evaluation of water stress in plants, or the evaluation of stress in the vegetation caused by water or atmosphere contaminants, among others [64–66]. Remote sensing allows one to see places that are difficult to access and allows for clarity when estimating changes or anomalies in the vegetation. For multispectral imagery, images from Landsat, Sentinel, or QuickBird satellites are commonly used [67,68]. Hyperspectral images are hardly ever used for this purpose according to the literature found.

Table A2 shows the development of the most common vegetation indices (VIs) over the last 50+ years; more IVs can be found at [69]. Among these, one of the first to be conceived was the Normalized Difference Vegetation Index (NDVI), which is attractive for its ability to rapidly delineate vegetation and vegetative stress. It is widely used in commercial agriculture and in land-use studies. For reasons related to its long history, its simplicity, and its reliance on readily available multispectral bands, the NDVI has become the most popular index used for vegetation assessment [70]. This index measures the relationship between the energy absorbed and emitted by plant covers through intensity values of the greenness of the area, the amount of vegetation present on a surface, and its state of health or vegetative vigor [71]. The NDVI relates the information acquired in the red and near-infrared (NIR) bands with the state and characteristics of the vegetation covers through the normalized difference of the two bands whose range of variation is between −1 and 1. Negative values (−1) to zero (0) are bare surfaces, while values from zero (0) to one (1) show the presence of plants [72]. Dense vegetation is given from values between 0.5 and 0.7 [73]. Another index used for vegetation is the Simple Relation Index

(SR), which reduces or eliminates the influence of the soil on solar reflectance values. It is considered as a structural index that allows for the estimation of leaf area index values [71]. On the other hand, the Soil-Adjusted Vegetation Index (SAVI) minimizes the effect of the soil on the characterization of the vegetation, especially on partially covered surfaces [71].

Different combinations of bands were made in order to analyze the most appropriate combinations for the study of the detection of pests in the vegetation between the Misantla and Coatepec coffee regions in the state of Veracruz, Mexico [73]. For this, Landsat satellite images with 11 bands were taken, with each one used to record the characteristics of surface objects such as soil, vegetation, and water. The methodology consisted of three main steps: obtaining digital images by flying a drone equipped with a multispectral sensor, characterizing the levels of the disease in a field-monitoring plot, and the digital processing of the images to obtain eleven vegetation indices compared in different levels of severity. These were evaluated from the Shapiro–Wilk, Levene, ANOVA, Kruskal–Wallis, and Wilcoxon statistical tests [74].

On the other hand, for studies carried out in areas affected by fires [75,76] as in Las Peñuelas in Moguer, Spain, vegetation indices were calculated for the evaluation of the recovery of plant vigor. In this case, cartographic maps were made that allowed one to observe the levels of recovery or retreat of the affected vegetation. Images from the Sentinel 2 and Pléaides satellites and images obtained in flyovers were used. Imagery was corrected for dark pixels produced by atmospheric scattering and then they compared with information obtained in the field to assess the reliability of the classification.

In general, Table A2 shows that IVs have their origins in the '60s–'70s and had their great development during the '90s and '00s. Although, in the last decade, new methodologies and advances have also been proposed. However, some fundamental aspects are evident. The first is that with technological advances, the concentration of researchers has focused on improving the quality of images with a greater number of bands in satellite sensors and smaller pixels on the ground. The second is that almost all the new indices have been developed in the United States, denoting a predominance of interest from the large universities and companies of this country on the subject, probably due to dominance over technology, the large extensions of vegetation in the country, and attention to environmental issues. Additionally, it was observed that the great concern was initially the reduction in atmospheric disturbance; however, with the arrival of specialized software on the subject, IVs have focused more on the preliminary identification of the state of the vegetation to correctly identify the use, timing, and dosage of treatments to intensify crop production, especially corn [77].

It is felt that the development of new indices is not as essential as in the past and that agreement has been reached on this. The academy and companies in the last decade have focused mainly on multitemporal studies of vegetation, evaluating water stress, and deforestation [78].

Other methodologies for the delimitation and calculation of vegetation areas are found with the use of spectral libraries that allow for the incorporation of new representative spectral signatures. For example, in Manaus, Brazil, Landsat satellite images were used, and the spectral library of urban materials based on categories of urban land cover components was created. The spectra that had a high probability of confusion with other classes of materials were eliminated and the most representative member of each class was chosen. To identify the most representative spectra of each class of material, the root mean square error (RMSE) was applied [79,80]. The end product of this analysis was a set of fractional abundance maps for each material class (i.e., vegetation, impervious surfaces, soil, and water). A similar methodology was applied in Yellowstone National Park, USA, which aimed at mapping the vegetation cover. In this study, a spectral library of reflectance signatures was created by pixel averaging over the known occurrences of 27 vegetation cover types in the study area [81].

Scopus showed that there were 43,651 works that included the words Remote sensing and Vegetation in the keywords, abstract, or title. Figure 3 shows the most common results

of the associated keywords. In terms of work frequency, the subject has had its greatest relevance in the last 20 years, probably due to greater attention to climate–environmental issues by institutions and companies. China, the United States, and Europe are the areas where the subject is most studied. Asia also plays an important role as China, India, and Japan are the dominant countries in these investigations, while Latin America again showed a trend that was similar to the case of asbestos.

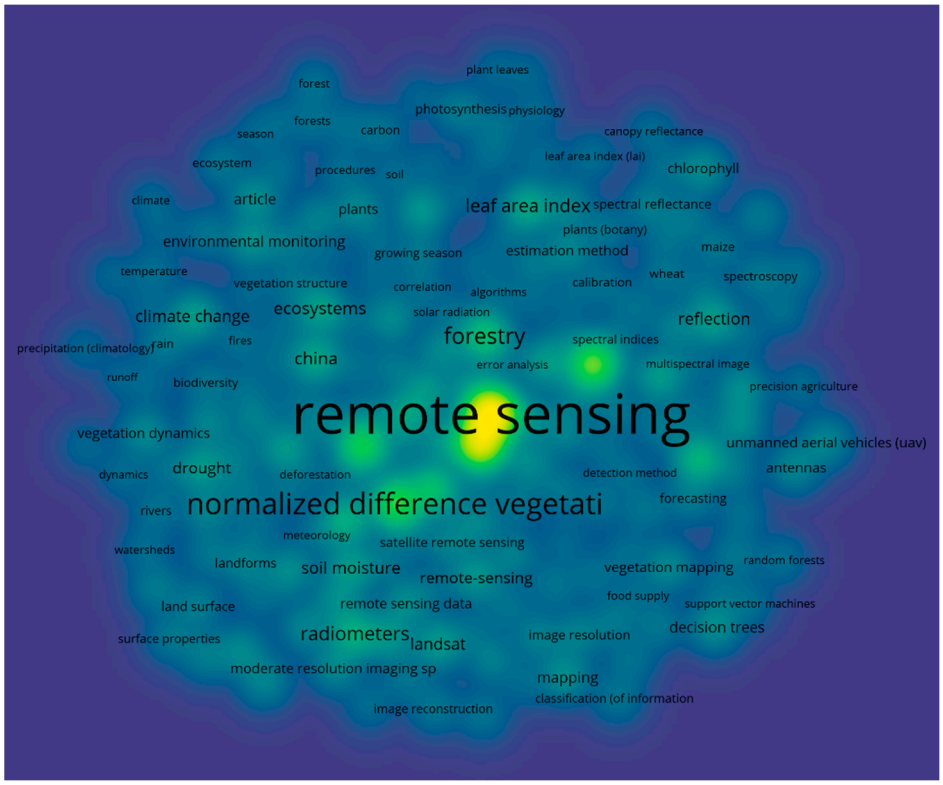

Figure 3. Keywords network found in Scopus searching with remote sensing and vegetation. Graph elaborated with VOSviewer.

5. Remote Sensing and Oil and Gas

Multispectral remote sensing is an emerging technology for the oil and gas industry. It has experienced an enormous advancement in relatively new fields such as geosciences for the exploration of hydrocarbons [82]. Remote sensing is a support tool for hydrocarbon exploration as it allows access to areas of physical inaccessibility, guaranteeing control of the threats caused by oil spills. Oil is an essential asset for societies; however, its transfer turns out to be difficult, since it is necessary to manage several transfers to take the hydrocarbons from the deposits to the refineries, the industries, and later the final clients [82]. During these transfers, spills may occur on land or in the water. In the latter case, waves, wind, and ocean currents can spread large slicks across open water in a matter of hours [83]. The early detection of anthropogenic oil slicks can enable the timely protection of critical habitats and limit economical damage [84].

In San Juan Capistrano, California, a remote sensing study was carried out in which the authors presented thermal infrared spectra of oil slicks made from five oil samples of different compositions. Different thicknesses of oil in water was tested in a laboratory to determine the reflectance spectra [85]. A similar methodology was applied by [86] in which three annual experiments of artificial mesocosms with oil in ice were carried out at the Sea Ice Environmental Research Facility (SERF) of the University of Manitoba, Canada, during 2016–2018 in order to see the behavior of oil in the ice.

On the other hand, in the Niger Delta (Nigeria) [87,88], Landsat images were acquired for the period of 2000–2018, and the NDVI was applied to determine the changes in

vegetation caused by oil spills. Another similar procedure was the case study in Deep Horizon (2012) and Campo Basin (2011), in which they used resolution images to monitor oil slicks using the fluorescence/emissivity index and image analysis, using a multispectral sensor 36-band with a resolution of 250 m to 1000 m on the EOS AM (Terra) and EOS PM (Aqua) satellites [89]. The study did not show acceptable results since oil does not have specific spectral characteristics that can be used for direct detection. However, in some circumstances, oil can have a silvery appearance with a reflectance higher than that of the background [82].

Another use of satellite images is that applied to the coast of Lake Albert (Africa), in which time series of multisensory satellites with images from 1999 to 2008 were used. These images were corrected for the atmosphere and radiometric calibration; subsequently, a comparison was made between the anomaly map generated by multisensor satellite images and the map with superimposed oil and gas fields. In the comparison, it was shown that all the anomalies are located in areas with high gravimetric gradients, so it was concluded that microleakage maps can provide new high-quality data, complementary to those of traditional geophysics, at an affordable cost and with no need for exploration licenses to help the oil and gas industry reduce exploration risk [82]. This methodology was also applied in Lake Turkana (Africa), in which satellite multispectral data were used to detect microfiltration signals. These were grouped into spectral anomalies according to land use, geographic, geological, and subsoil variables. The study gave good results since an underground accumulation of hydrocarbons was evidenced [90].

Scopus showed that works with the keywords remote sensing and oil and gas were not very frequent as 1176 documents were found, which was probably because most of the works were carried out by private companies that do not publish their results due to issues related to copyright, patents, and industrial secrets, as this is a strategic economic sector. Appendix A reports some of the most relevant papers on the matter, confirming that most of them are related to hydrocarbon seepage. Once again, the United States and China led the investigations, followed by the Russian Federation.

6. Geology Applications

Remote sensing has become a very important instrument, being used in various investigations related to the identification of minerals [91–93], lithology mapping [94–96], and environmental geology due to contamination by mining areas [97]. Mineralogical studies and lithological mapping have been performed in different climatic and tectonic conditions where hyperspectral imaging for VNIR and SWIR spectral ranges is common [98]. Nevertheless, according to [99], most minerals are identifiable in the SWIR and Long Wavelength Infrared (LWIR) ranges.

The basis on which a spectral processing technique requires a priori reference data or not is used to establish a categorization scheme. In the case of no reference data, the method is usually able to directly use the available spectral patterns in a pixel (or measured spectra). Additionally, there are techniques that try to describe the spectral content of a pixel according to some predefined representative facts, known as reference data or endmembers. This initial difference gives rise to two different categories: the knowledge-based approach and the data-driven approach, which contain different classifiers [100].

Other forms for the identification of mineral assemblages is from relation indices, similar to the case of vegetation indices [101]. The Index Data Base (IDB) is a tool for working with remote sensing indices available on the web [69,102]. It provides a quick overview of which indices are usable for a specific sensor and a specific topic. It is a valuable tool for indices developed before 2012 based on the Advanced Spaceborne Thermal Emission and Reflection Radiometer sensor (ASTER), 15 bands from 520–11,650 μm, resolution of 15–90 m. Carbonate, clay, ferric iron, and SiO_2, among many other indexes to identify minerals, are reported in the literature. Clearly, for this type of large-scale application, high resolution is not needed. The use of hyperspectral images with a spatial resolution of less than 30 cm is possible thanks to modern technology; however, the information requires

extraordinary storage and a consequent computational capacity that is not very accessible at a commercial level.

An applied step in methodologies for geology that can be diligent within other disciplines would be the use of Linear Spectral Unmixing (LSU) classifiers, which is a spectral unmixing tool that decomposes a reflectance source spectrum into a set of end-member spectra. This classifier showed better results compared to others that were used. According to [91], the LSU indicates a better technique for estimating the distribution of pure and impure pixels compared to methodologies such as SAM and SFF that classify all pixels as pure when they are actually impure. Another technique that performs a partial unmixing of spectra is the CEM algorithm, applied by [103], which is considered a powerful sub-pixel demixing analysis tool for analyzing ASTER reflectance data.

Machine learning algorithms are known because they work from training data sets. In a study carried out by [104] to obtain a lithological map in the greenstone belt of the Hutti area, India, the impact of the quantity on the performance of these algorithms was evaluated, for which a reduction of 15%, 30%, and 45% was made of the total samples, showing that there was a slight reduction in the global accuracies. In the case of LDA, the precision was reduced by 5%, in RF by 2%, and in SVM by 1%, thus showing that the least sensitive method to the size of data sets was SVM compared to the other two. This statement was validated in other studies [105], where SVM showed better results than other methodologies such as SAM using a relatively low number of sampling data. However, the SVM method is not widely used for lithology mapping; it is an effective algorithm for remote predictive mapping for remote areas as well as for updating existing lithology maps. It generates a high precision of up to 85% as in the lithological cartography of the Souk Arbaa Sahel region belonging to the Sidi Ifni located in southern Morocco [106].

Over time, new methodologies that are different from the conventional ones have been applied, such as the Convolutional Neural Networks (CNNs), which have presented better results. The authors of [96] presented a comparison of this methodology based on other conventional methodologies such as SAM, SID, FCLSU, SVM, and RF, showing that two-dimensional CNNs and three-dimensional CNNs were approximately 2.5–12% higher than that of SVM and RF and approximately 12−25% higher than that of SAM, SID, and FCLSU. Therefore, the CNN 2D and CNN 3D algorithms improve the classification of hyperspectral TIR remote sensing images, as it offers a better classification performance, higher noise immunity, and more accurate boundary classification. It should be noted that with this method, the global accuracies were up to 98.56%. Despite other classification methodologies being better for the identification of minerals and the generation of lithological maps such as SVM, RF, and CNN, the most used classifier is SAM which, as mentioned above, does not work very well when there are not enough training data [28,96,107]. In geological studies, it is quite difficult to obtain a lot of training data due to difficult access areas as in the case of [105] where a lithological map of an area formed by the Teide-Pico Viejo stratovolcano was made.

In unsupervised classification techniques, where classes are created purely based on spectral information and not manual visual interpretation, methods such as K-means and the Iterative self-organizing method (ISODATA) are most common. However, this topic is outside the scope of this work.

Geological applications of remote sensing are among those that have generated interest in researchers and companies since the 1980s, aimed at characterizing and monitoring large extensions of soil, the search for precious minerals, and lithological studies. Appendix A shows a summary of the most relevant and mentioned works in the literature on the subject. It can be noted that this field has the greatest variety of applications, mostly focused on the identification of minerals; however, there are also more advanced applications, such as in structural geology, crustal deformation, and geological lineaments. Scopus shows that there are 16,326 works to date with the words “Remote sensing” and “Geology”. Figure 4 shows the most common results of the associated keywords. In terms of the frequency of keywords, the same frequencies per country are evident as in the case of asbestos,

vegetation, and oil and gas. On the other hand, relationships between geological and geotechnical studies with climate change, glacial geology, risk, and landslides are noted.

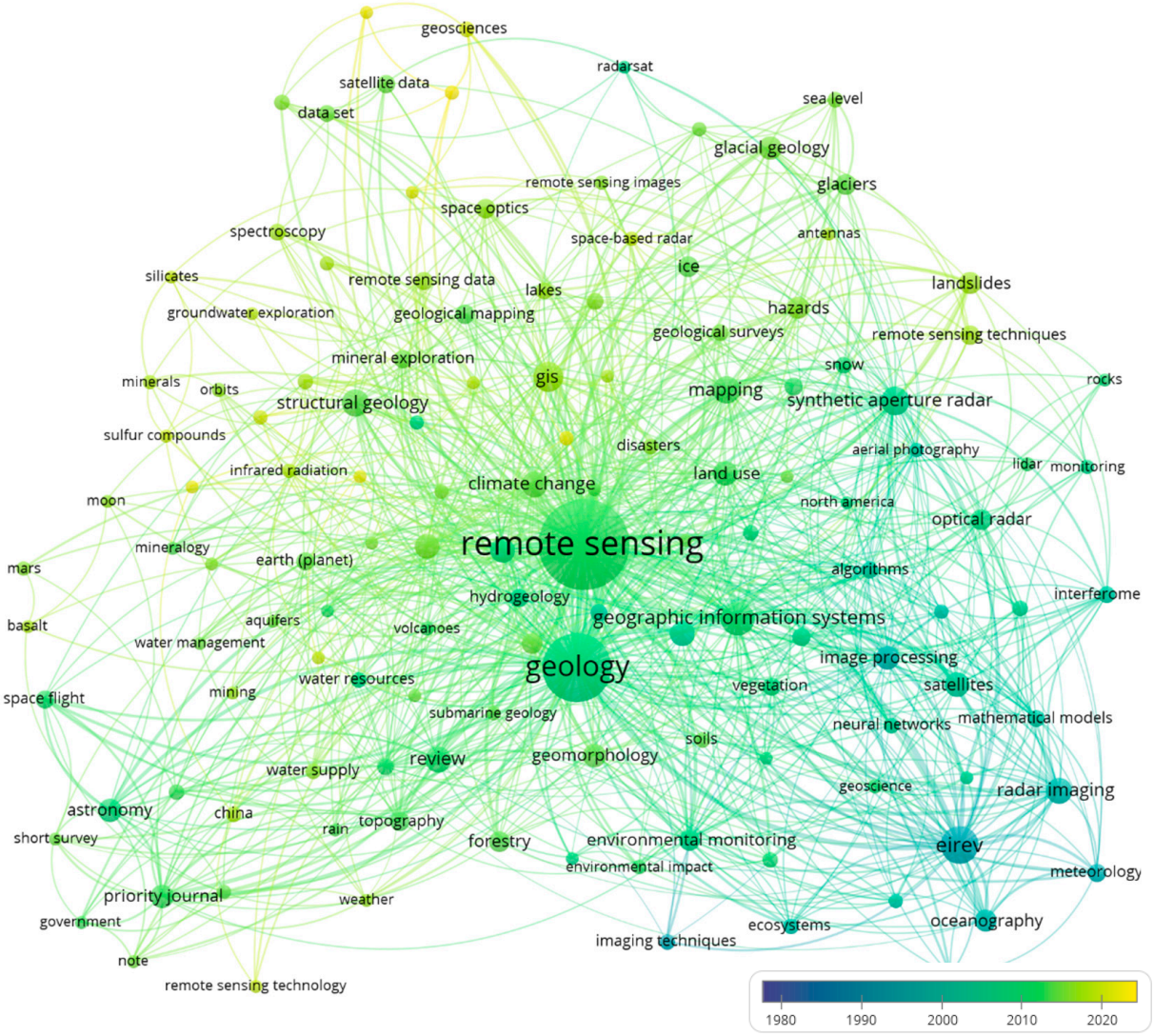

Figure 4. Keywords found in Scopus while looking for works with the keywords "Remote sensing" and "Geology". Graphic made with VOSviewer.

7. Spectral Signature

One of the key points in remote sensing studies in any of its fields of application is the response of materials to the incidence of a light ray and their identification through the spectral signature [49]. Each material has a different spectral signature, which varies depending on its physical–chemical and morphological characteristics and its capacity to absorb, transmit, or reflect the energy received. The latter is measurable through reflectance as a function of wavelength [108]. The most reflective part of the electromagnetic spectrum is in the wavelength range of 350 nm to 2500 nm, so it is within these values that most remote sensing research and applications are carried out [109].

Figure 5 shows some of the spectral signatures that can be found in the fields of application mentioned above: asbestos, vegetation, oil and gas, and soil. Most of these spectral signatures can be found in the U.S. Geological Survey (USGS) spectral library, made with laboratory, field, or aircraft-mounted spectroradiometers and covering the spectrum from 200 nm to 200,000 nm depending on the measurement performed [110].

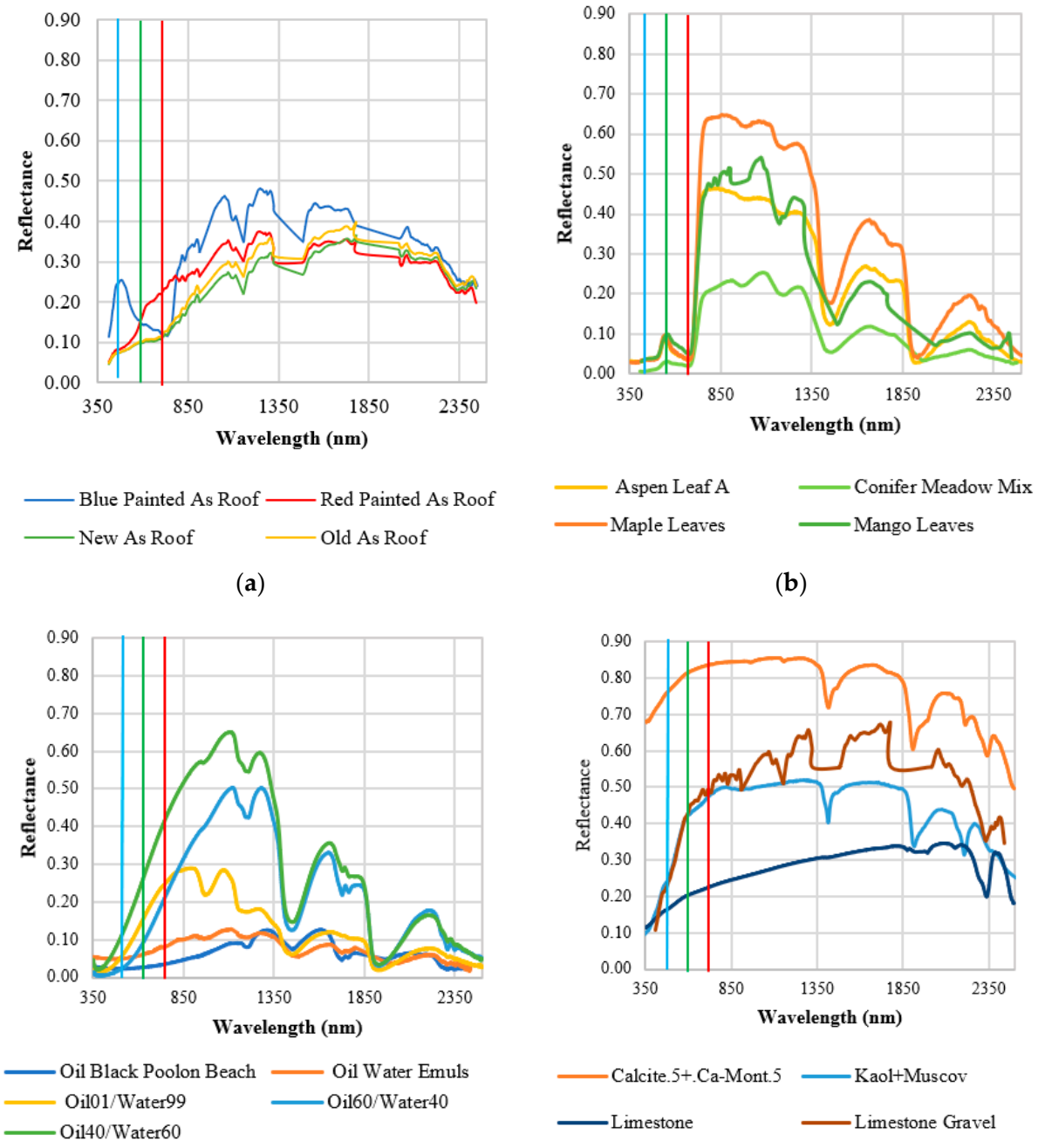

Figure 5. Spectral signatures of some materials within the categories: (**a**) asbestos, (**b**) oil and gas, (**c**) vegetation, and (**d**) soil. Vertical lines represent blue, green and red area of the spectrum. Reflectance can vary from 0 to 1.

The spectral signatures of asbestos are part of an ongoing investigation by the authors, where an aircraft mounted with a HySpex V620 hyperspectral sensor was used to collect the information. Asbestos, having different types of fibers, can present different spectral signatures according to the material under study; however, the greatest variations in reflectance occurred near the SWIR wavelengths between 1195 to 1415 nm and between 1742 and 1974 nm, which makes this range quite useful in its identification by means of classification tools such as SAM or SVM [111]. The state of deterioration and type of asbestos fibers significantly modify the spectral signature [63,112]. Asbestos–cement roofs with a nondeteriorated cement matrix may present greater energy reflection; on the contrary,

those painted or protected with waterproofing usually have lower energy reflection [63,112]. Figure 5a shows some spectral signatures of asbestos–cement roofs in the city of Cartagena, Colombia. Higher reflectance values in the NIR and SWIR zones were observed, with some reflectance peaks near 1080, 1250, and 1550 nm. However, low spectral values in the visible range could differ significantly, while the spectral values for longer wavelengths are similar. Some asbestos–cement ceilings were painted different colors, and this produced an effect on the spectral signature of this material, reflecting a high reflectance near the ranges corresponding to the color; in the case of a blue ceiling, there was a modification that was significant near 490 nm, and for the red ceiling, an increase in reflectance was seen from 620 nm to 900 nm, passing from the green band to the first part of the near infrared. In both cases, the spectral signature maintained its shape, but with higher reflectance values.

In the case of the oil and gas industry, the application of remote sensing for the identification of contamination from oil spills has been of the utmost importance. During these events, it is necessary to know where the contaminant moves in the water and the magnitude of the places affected. In an investigation performed by [113] on an oil spill from the Deepwater Horizon platform in Barataria Bay, Louisiana, the authors found that the oil spectral signature was affected according to the materials that were in the background, such as water, sediment, or vegetation. Figure 5b shows the series "Oil Black Poolon Beach" and "Oil Water Emuls", where the difference between them was that the first one was on beach sand and the second one was in the water. Another important factor is the mixing ratio and the thickness of the oil layer, both of which can cause the oil to emulsify and therefore change the spectral signature. In the same event as the Deepwater Horizon spill, the authors of [114] found that the proportion of oil:water that yielded the highest reflectance values was 40:60 and that the thickness of the layers, even if they varied by a few millimeters, caused the reflectance to vary considerably.

The vegetation, for its part, presented low values of reflectance in the visible range, except for a peak near 500 nm where the green band is located; this was due to the photosynthesis processes of the plants that absorbed most of the energy in the other wavelengths. However, advancing in the spectrum, near 700 nm where it is known as the "red-edge region", the spectral signature increased the reflectance values, maintaining a similar trend until crossing the midinfrared, where there was a large absorption of energy due to the water content in the plants. Again the reflectance values rose in the SWIR area [115]. It is for this reason that the vegetation indices are mostly related to red and near-infrared wavelengths and some more recent ones use SWIR for applications of nonphotosynthetic processes [116]. In Figure 5c, the typical behavior of vegetation in four different species, i.e., Aspen Leaf A (Denver, CO [110]), Conifer Meadow Mix (Yellowstone Park [81]), Maple Leaves (Golden, CO [110]), and Mango Leaves (Cartagena, Colombia) is observed, in which the reflectance values vary but the trend and shape of the spectral signatures are similar to each other. These changes in reflectance allow one to know the type of vegetation under study and contribute to analyzing changes within the vegetation, such as the stress levels, leaves' health, and overall quality of the vegetation [117,118].

The soils presented higher reflectance values than the other categories in the entire spectrum. They tended to reflect electromagnetic energy in a greater proportion. Most of the time it was related to the chemical composition of the soil under study and its relationship with the ecosystem in which it was found [118–120]. The characteristics of each type of soil made it possible to find some absorption peaks in the spectral signature. In Figure 5d, it is observed that the greatest energy absorption was found in the SWIR part; however, the highest reflectance values were maintained in this area. In the case of the Calcite.5+.Ca-Mont.5 (mixture of Calcite and Montmorillonite) and Limestone signatures, the authors of [110] describe that the absorptions in the SWIR are related to the interaction of C-O within the chemical composition and some organic impurities of the materials, giving the signature a negative slope in this short wave zone. A similar effect also occurred for Kaol + Muscov (mixture of Kaolinite and Muscovite), where it was observed that a band was highly influenced by Muscovite in the 2200 nm zone. These patterns can explain

the behavior of the Limestone Gravel series, from the city of Cartagena, which presented combinations of the first two materials mentioned.

8. Conclusions

In this work, world trends on remote sensing related to some of the most relevant issues at the global level were studied. In particular, the present manuscript focused on public health problems in the case of asbestos; environmental issues in the case of vegetation and oil and gas, in addition to hydrocarbon exploration; and geological applications in the case of the identification and characterization of soils and minerals. Several aspects that are worth highlighting were evidenced. Remote sensing studies related to vegetation were the studies most frequently found in the literature, with a marked tendency for researchers in the 1990s and 2000s to create new vegetation indices (Figure 6). More than 30 indices were found among the most relevant and mentioned studies in the literature, which are useful for different applications. However, no recent studies were found that would allow all the indices to be compared with each other in the same multispectral or hyperspectral image. In the latter case, it is probably due to the scarcity of satellite hyperspectral sensors and their cost/logistics for use in drones or manned aircraft.

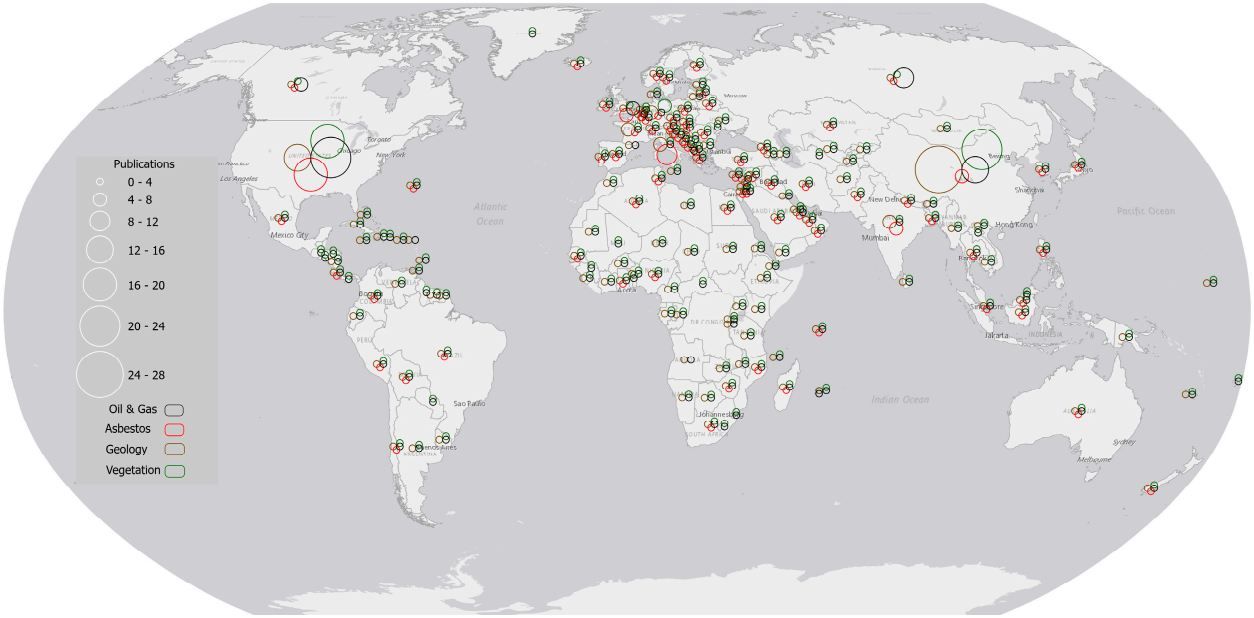

Figure 6. Summary of publications by country on oil and gas (black), asbestos (red), geology (brown), and vegetations (green).

In terms of public health, the applications for the detection of asbestos–cement roofs are interesting. Developing countries that are barely banning the use of this material have multispectral satellite images available, such as those from Word View 3 (WV3), to be able to identify asbestos–cement roofing. Since 2020, these have had a reasonable SRE for SWIR (~3.7 m). However, with this tool, countries that have also banned the material decades ago can track the progress of removal. It is evident that this technology of the WV3, with its 8 VNIR bands and 8 SWIR bands, is also useful for other applications. The main limitation in this case is cloudiness, which in some areas is constant throughout the year; however, images can be taken upon request with a limit to the percentage of cloudiness. More studies are needed to investigate the efficiency of cover identification through multispectral satellite imagery and hyperspectral flyby imagery. Since these studies are on urban areas, the overflights have the limitation of urban airports, or military areas, with restrictions in the landing cone and surrounding areas. Finally, remote sensing applied to oil and gas is a subject that has not been studied much; however, it has great potential as a tool to support

preliminary studies for the exploration of wells to find hydrocarbons. As mentioned, this lack of published studies probably reflects the need for companies in the sector to keep information and methodologies confidential.

9. Recommendations

The results highlighted in the present review are relevant for environmental policymakers. Remote sensing should be applied in problem identification, policy formulation, policy implementation, and policy control and evaluation to strengthen governance and improve policy efficiency and effectiveness. For instance, in the case of asbestos–cement roofs, better strategies for removing and wasting can be tailored if roof distribution has been previously categorized. On the other hand, great economic development has characterized entire economic sectors after asbestos prohibition, and private companies should encourage remote sensing in urban areas to customize roof replacement options and optimize position of the disposal sites.

Air quality and quality of life in urban environments are in part related to the presence of green areas. Policymakers and environmental engineering companies should promote multitemporal remote sensing analysis to control and improve vegetation in urban environments, especially in underdeveloped countries where the population density and building speculations are extreme. Similar to the case of oil slick identification, permanent control with remote sensing will help prevent the spread of environmental disasters, especially in remote areas of developing counties.

Finally, remote sensing should change paradigms in policymakers and companies since inversions in this technology and these images may generate high returns in terms of quality of life and environmental quality, maximize the resources to explore the raw materials, and minimize the costs of mitigating environmental problems.

Author Contributions: Conceptualization, M.S. and L.K.T.G.; methodology, M.S.; formal analysis, L.K.T.G., D.V.M. and M.S.; investigation, L.K.T.G., D.V.M. and M.S.; resources, L.K.T.G., D.V.M. and M.S.; data curation, M.S.; writing—original draft preparation, L.K.T.G. and M.S; writing—review and editing, L.K.T.G., D.V.M. and M.S.; visualization, L.K.T.G., D.V.M. and M.S; supervision, M.S.; project administration, M.S.; funding acquisition, M.S. All authors have read and agreed to the published version of the manuscript.

Funding: This research was funded by General System of Royalties of Colombia (SGR) grant number BPIN 2020000100366. And the APC was funded by the University of Cartagena, project approved by the resolution N. 01385 od 2021.

Institutional Review Board Statement: Not applicable.

Informed Consent Statement: Not applicable.

Data Availability Statement: Not applicable.

Acknowledgments: This article is considered a product in the framework of the project "Formulation of an integral strategy to reduce the impact on public and environmental health due to the presence of asbestos in the territory of the Department of Bolivar", financed by the General System of Royalties of Colombia (SGR) and identified with the code BPIN 2020000100366. This project was executed by the University of Cartagena, Colombia, and the Asbestos-Free Colombia Foundation. Finally, the authors thank Daniela Velez Clavijo and María Angélica Márquez de León for their invaluable support.

Conflicts of Interest: The authors declare no conflict of interest.

Appendix A

Table A1. The most relevant studies for asbestos roofing identification, oil and gas, and geology related to remote sensing found in literature in the last decade, identified by relevance and organized in increasing order by year.

Material	Location	Image Taking Tool	Type of Sensor/Satellite	Number of Bands	Ground Resolution	Methodology	Year	Ref.
Asbestos	Follonica and Rimini, Italy	Overflight	MIVIS	102	3.0–4.0 m	Spectral Angle Mapper (SAM)	2008	[118]
Asbestos	Rome, Italia	Overflight	MIVIS	102	4.0 m	Spectral Angle Mapper (SAM)	2012	[57]
Asbestos	Hyderabad, India	Satellite	QuickBird	3	Panchromatic = 0.61–072 m; VNIR = 2.44–2.88 m	PCA-based; line-detection-based	2012	[119]
Asbestos	Barcelona, Spain	Overflight	Hyperspectral	32	2.0–2.4 m	Integration of rooftop greenhouses	2017	[120,121]
Asbestos	Lombardía, Italy	Overflight	MIVIS	102	3.0 m	Spectral Angle Mapper (SAM)	2018	[54]
Asbestos	Debrecen, Hungary	Satellite	WorldView-2	8	Panchromatic = 2 m VNIR= 0.5 m	LDFA = Linear Discriminant Function Analysis; QDFA = Quadratic Discriminant Function Analysis; RF = Random Forest;	2018	[56]
Asbestos	Prato, Italy	Satellite	WorldView-3	16	Panchromatic = 0.31 m; VNIR = 1.24 m; SWIR= 3.70 m	QGIS Plugin named RoofClassify	2019	[30]
Asbestos	Chęciny, Poland	Overflight	Orthophotomap	3	0.25 m	Convolutional Neural Networks (CNNs)	2020	[44]
Asbestos	São José do Rio Preto, Brazil	Satellite	WorldView-3	16	Panchromatic = 0.31 m; VNIR = 1.24 m	Maximum likelihood, mahalanobis distance, and minimum distance.	2020	[122]
Asbestos	Chęciny and Baranów, Poland	Overflight	Orthophotomap	3	0.25 m	Convolutional Neural Networks (CNNs)	2022	[123]
Asbestos	Paldal-dong, Daegu, South Korea	Overflight	Orthophotomap	NA	NA	Visual counting method	2022	[124]

Table A1. *Cont.*

Material	Location	Image Taking Tool	Type of Sensor/Satellite	Number of Bands	Ground Resolution	Methodology	Year	Ref.
Exploration of oil	Southern Tunisia	Satellite	Landsat Enhanced Thematic Mapper (ETM+); ASTER Red–Green–Blue (RGB) radar (RADARSAT)	See the reference	10 m to 100 m	Interpretation of the Shuttle Radar Topography Mission (SRTM) Digital Elevation Models (DEMs)	2006	[125]
Hydrocarbon seepages	Campos Basin, Brazil and Bay of Campeche, SE Gulf of Mexico	Satellite	ASTER	9	VNIR= 15 m; SWIR= 30 m; Thermal Infrared (TIR) = 90 m.	Spectral processing of the data; selection and preprocessing (e.g., atmospheric compensation) of ASTER imagery containing seepage records; mapping the extension of oil over water through some classification scheme (e.g., Fuzzy Clustering); selection of representative spectra from seepage pixels extracted from ASTER imagery; integration of multivariate statistics processing.	2012	[126]
Exploration of oil	Louisiana (USA) (Deep Horizon) and Campo Basin, Brazil	Satellite	EOS AM (Terra) and EOS PM (Aqua) Moderate-Resolution Imaging Spectroradiometer (MODIS)	36	250–1000 m	Object-based image analysis (OBIA)	2014	[87]

Table A1. *Cont.*

Material	Location	Image Taking Tool	Type of Sensor/Satellite	Number of Bands	Ground Resolution	Methodology	Year	Ref.
Gas leak	Kelowna, Canada	Unmanned aerial vehicle (UAV)	Laser Methane mini-G SA3C50A	NA	Not specified. Flight altitudes: 25–30 m	Off-the-shelf laser-based methane detector into a multirotor UAV	2017	[127]
Hydrocarbon seepages	Gulf of Mexico	Satellite	RADARSAT-2; ASTER and WorldView-2	See the reference	1–15 m	Oil/emulsion thickness classification using Satellite Synthetic Aperture Radar (SAR)	2020	[128]
Gas leak	Katowice, Poland	Unmanned aerial vehicle (UAV)	LaserMethane mini SA3C321-BE	NA	Not specified. Flight altitudes: 3.5 m, 6 m, 9 m, 12 m, 15 m, 18 m, 21 m, and 25 m	Data cleaning; background/leakage gas concentration determination; location of the leakage estimation.	2021	[129]
Hydrocarbon seepages	Sudd Wetlands in South Sudan	Satellite	Sentinel-1; Sentinel-2	13	10–60 m	Random Forest (RF)	2021	[130]
Hydrocarbon seepages	Louisiana (USA) (Deep Horizon)	Satellite	Sentinel-1 and RADARSAT-2	Not specified.	Sentinel-1 = 20m; RADARSAT-2 = 50 m	Faster Region-based Convolutional Neural Network (Faster R-CNN) model	2022	[131]
Hydrocarbon seepages	Matruh Basin, Egypt	Satellite y Hyperspectral	EO-1 (ALI) and Landsat-7; EO-1 (HYPERION)	6; 4; 49; 49	30 m for all sensors	Spectral Angle Mapper (SAM)	2022	[132]
Gold exploration	Southeastern Desert of Egypt	Satellite	ASTER and ETM+	6	Not specified	Band ratioing, principal component analysis (PCA), false-color composition (FCC), and frequency filtering (FFT-RWT)	2012	[133]

Table A1. *Cont.*

Material	Location	Image Taking Tool	Type of Sensor/Satellite	Number of Bands	Ground Resolution	Methodology	Year	Ref.
General mineral identification	Girón, Colombia	Satellite	Hyperion- Satellite EO-1	220	30 m	Spectral Angle Mapper (SAM)	2015	[134]
Geologic mapping	Edembo area, Algerian Sahara	Satellite	Multispectral ASTER	9	VNIR = 15 m; SWIR = 30 m; thermal infrared (TIR) = 90 m.	Maximum likelihood classifier method (MLC)	2016	[135]
Map alteration minerals	Southeast Spain	Satellite	WorldView-3 imagery and ASTER TIR	See the reference	Panchromatic = 0.31 m; VNIR = 1.24 m; SWIR = 3.70 m TIR =90 m.	Spectral Angle Mapper (SAM)	2019	[48]
Groundwater exploration	Gongola Basin, Nigeria	Satellite	Landsat 8	3	Not specified	Detection of lineaments through geophysical gravity	2020	[136]
Mineral exploration	Semna region, Eastern Desert (ED) of Egypt	Satellite	Multispectral ASTER	9	VNIR = 15 m; SWIR = 30 m; thermal infrared (TIR) = 90 m.	The ASTER data were enhanced in terms of mapping lithological units and the hydrothermal zones	2010	[137]
Kimberlite exploration	Kimberlite Province, Lesotho	Satellite	ASTER, Shuttle Radar Topography Mission (SRTM) Digital Elevation Model (DEM) and Google Earth	9	VNIR = 15 m; SWIR = 30 m	Spectral Angle Mapper (SAM)	2021	[138]
Iron mineral	Çankırı Province, Turkie	Satellite	Sentinel-2	13	5, 30 and 60 m	Spectral Angle Mapper (SAM)	2021	[139]
Structural framework and mineral occurrences	Nimas-Khadra, Southern Arabian	Satellite	ASTER	14	VNIR = 15 m SWIR = 30 m TIR = 90 m	Geophysical and image analyses to identify the tectonic framework and establish the relationship of the lithology and tectonic features with the known and prospective mineral occurrences	2022	[140]

Table A1. *Cont.*

Material	Location	Image Taking Tool	Type of Sensor/Satellite	Number of Bands	Ground Resolution	Methodology	Year	Ref.
Structural geology measurements of lava flows	Lake Assal, Djibouti	Satellite	Pleiades	5	0.5 m	Mouse Mode (MM) and Virtual Reality (VR) approaches	2022	[141]
Crustal deformation	Niger Delta Basin	Satellite	Landsat 8, Advanced Land Observation Satellite (ALOS), World 3D DEM	See the reference	30 m	Integration of satellite images	2022	[142]
Geological lineaments	Central Turkey	Satellite	Landsat 8; Advanced Land Observing Satellite (ALOS)	8	30 m; 10–100 m	Preprocessing of both optical and radar images, the image enhancement, and the determination of optimal parameter values employed in the extraction of lineaments from the data sets and the verification and the interpretation of the resultant lineament maps	2022	[143]

MIVIS = multispectral infrared visible imaging spectrometer; ASTER = Advanced Spaceborne Thermal Emission and Reflection Radiometer.

Table A2. The most relevant vegetation indices found in literature.

Vegetation Indices (VIs)	Formulas	Study Area	Observations	Year	Ref.
Simple Ratio	SR = NIR/Red	Marysville, USA	A two-wavelength reflectance ratio R745/R675 was developed for an objective index of turf color	1968	[144]
Normalized Difference Vegetation Index	NDVI = (NIR − Red)/(NIR + Red)	Texas, USA	Multispectral satellite images are used. A method has been developed for quantitative measurement of vegetation conditions over broad regions using ERTS-1 MSS data	1974	[145]
Green Vegetation Index	GVI = (−0.2848 TM1) + (−0.2435 TM2) + (−0.5436 TM3) + (0.7243 TM4) + (0.0840 TM5) + (−0.18 TM7)	Worldwide	This index minimizes the effects of background soil while emphasizing green vegetation. It uses global coefficients that weigh the pixel values to generate new transformed bands. It is also known as the Landsat TM Tasseled Cap green vegetation index	1976	[146]
Difference Vegetation Index	DVI = NIR-Red	Maryland, USA	In situ collected spectrometer data were used	1979	[147]
Soil-Adjusted Vegetation Index	SAVI = (1.5 (NIR − Red))/(NIR + Red + 0.5)	Arizona, USA	Similar to NDVI; nevertheless, it is a proposed index that minimizes soil brightness influences involving red and near-infrared (NIR) spectra	1988	[148]
Infrared Percentage Vegetation Index	IPVI = NIR/(NIR + Red)	Worldwide	The near-infrared (NIR) versus red "infrared percentage vegetation index," NIR/(NIR + Red), is functionally and linearly equivalent to the Normalized Difference Vegetation Index, (NIR-Red/(NIR + Red). Advantageously, it is both computationally faster and never negative	1990	[149]
Global Environmental Monitoring Index	GEMI = η (1 − 0.25 η) + (Red − 0.125)/(1 − Red) η = 2(NIR^2 − Red^2) + 1.5NIR + 0.5Red)/(NIR + Red + 0.5)	Worldwide	Designed specifically to reduce the relative effects of these undesirable atmospheric perturbations	1992	[150]

Table A2. *Cont.*

Vegetation Indices (VIs)	Formulas	Study Area	Observations	Year	Ref.
Atmospherically Resistant Vegetation Index Difference Vegetation	$ARVI = (NIR - (Red - \gamma(Blue - Red)))/(NIR + (Red - \gamma(Blue - Red)))$	Worldwide	MODIS sensor. ARVI has a similar dynamic range to the NDVI but is on average four times less sensitive to atmospheric effects than the NDVI	1992	[151]
Modified Soil-Adjusted Vegetation Index 2	$MSAVI2 = (2\ NIR + 1-\sqrt{((2\ IR + 1)-8\ (NIR-Red)))})/2$	Tucson, USA	This index is a simpler version of the MSAVI proposed by Qi et al. (1994), which improves upon the Soil-Adjusted Vegetation Index (SAVI). It reduces soil noise and increases the dynamic range of the vegetation signal. MSAVI2 is based on an inductive method that does not use a constant L value (as with SAVI) to highlight healthy vegetation [152]	1994	[153]
Nonlinear Index	$NLI = (NIR^2 - Red)/(NIR^2 + Red)$	Detroit, USA	Multispectral satellite images are used. A comparison between 3D crop model and several VIs is proposed focusing on soil brightness, optical properties of canopy elements, leaf angle distribution, and spacing, among others. The authors found that VIs using off-nadir reflectances are more informative and useful than those based on nadir reflectances; the optimal VI and sun/view geometries are usually different for inferring different parameters, depending on canopy architecture; and LAI can be practically estimated by VI only for homogeneous canopies	1994	[154]

Table A2. *Cont.*

Vegetation Indices (VIs)	Formulas	Study Area	Observations	Year	Ref.
Renormalized Difference Vegetation Index	RDVI = (NIR − Red)/$\sqrt{}$(NIR + Red)	Toulouse, France	Similar to NDVI; nevertheless, a VI to minimize soil effects is proposed	1995	[155]
Structurally Independent Pigment	SIPI = (NIR–Blue)/(NIR–Red)	Barcelona, Spain	The index minimizes the confounding effect of leaf surface and mesophyll structure	1995	[156]
Optimized Soil-Adjusted Vegetation Index	OSAVI = (NIR − Red)/ (NIR + Red + 0.16)	Nottingham, UK	Similar to NDVI; nevertheless, the value of the parameter X is critical in the minimization of soil effects. A value of 0.16 is proposed	1996	[157]
Green Atmospherically Resistant Index	GARI = (NIR – [Green-γ(Blue – Red)])/ (NIR + [Green-γ(Blue – Red)])	Worldwide	MODIS sensor. GARI is tailored to the concept of ARVI. Resistant to atmospheric effects as ARVI but more sensitive to a wide range of Chl-a concentrations. While NDVI and ARVI are sensitive to vegetation fraction and to rate of absorption of photosynthetic solar radiation, a green vegetation index such as GARI should be added to sense the concentration of chlorophyll, to measure the rate of photosynthesis, and to monitor plant stress.	1996	[158]
Modified Simple Ratio	MSR = ((NIR/Red) − 1)/ ($\sqrt{}$(NIR/Red) + 1)	Ottawa, Canada	Multispectral satellite images are used to classify boreal forests. They evaluate several vegetation indices against experimental data sets for their performance in terms of the ability to minimize the error induced by noise in remote sensing data. The authors propose a nonlinear index that has the advantage of both low noise effects and good linearity with biophysical parameters	1996	[159]

Table A2. *Cont.*

Vegetation Indices (VIs)	Formulas	Study Area	Observations	Year	Ref.
Green Normalized Difference Vegetation Index	GNDVI = (NIR − Green)/NIR + Green)	Worldwide	Satellite images for remote sensing of chlorophyll concentration	1998	[160]
Green Leaf Index (GLI)	GLI = ((Green – Red) + (Green – Blue))/ (2*Green + Red + Blue)	Oregon, USA	This index was originally designed for use with a digital RGB camera to measure wheat cover, where the red, green, and blue digital numbers (DNs) range from 0 to 255 GLI values range from −1 to +1. Negative values represent soil and nonliving features, while positive values represent green leaves and stems [152].	2001	[161]
Enhanced Vegetation Index	EVI = 2.5 (NIR-Red)/(NIR + (6 Red) − (7.5 Blue) + 1)	Worldwide	The study was performed using the Moderate Resolution Imaging Spectroradiometer (MODIS), which is a 36-band imaging radiometer, on the NASA Earth Observing System (EOS) satellites Terra [162]	2002	[163]
Leaf Area Index	LAI = 3.618 × EVI – 0.118	Denmark	Multispectral data were acquired with the Compact Airborne Spectral Imager (CASI). The results allowed for the evaluation of the spatial variations in the photosynthetic light, nitrogen, and water use efficiencies. While photosynthesis was linearly related to transpiration, the light use efficiency (LUE) was found to be dependent on nitrogen concentrations	2002	[164]

Table A2. *Cont.*

Vegetation Indices (VIs)	Formulas	Study Area	Observations	Year	Ref.
Visible Atmospherically Resistant Index	VARI = (Green − Red)/(Green + Red − Blue)	Nebraska, USA	The goal of this study was to investigate the information content of reflectance spectra of crops in the visible and near-infrared range of the spectrum and develop a technique for remote estimation of vegetation fraction	2002	[165]
Transformed Difference Vegetation Index	TDVI = 1.5((NIR-Red)/$\sqrt{(NIR^2 + Red + 0.5)}$)	Ottawa, Canada	This index shows the same sensitivity as the Soil-Adjusted Vegetation Index (SAVI) to the optical properties of bare soil subjacent to the cover. It does not saturate like NDVI and SAVI and it shows an excellent linearity as a function of the rate of vegetation cover	2002	[166]
Green Chlorophyll Index	GCI = (NIR + Green) − 1	Lincoln, USA	This index is used to estimate leaf chlorophyll content across a wide range of plant species. Having broad NIR and green wavelengths provides a better prediction of chlorophyll content while allowing for more sensitivity and a higher signal-to-noise ratio [152]	2003	[167]
Sum Green Index	SGI = Green	California, USA	SGI is the mean of reflectance across the 500 nm to 600 nm portion of the spectrum. The sum is then normalized by the number of bands to convert it back to units of reflectance. The value of this index ranges from 0 to more than 50 (in units of % reflectance). The common range for green vegetation is 10 to 25 percent reflectance [152].	2003	[168]

Table A2. *Cont.*

Vegetation Indices (VIs)	Formulas	Study Area	Observations	Year	Ref.
Wide Dynamic Range Vegetation Index	WDRVI = (a NIR-Red)/(a NIR + Red)	Lincoln, NE, USA	This index is similar to NDVI, but it uses a weighting coefficient (a) to reduce the disparity between the contributions of the near-infrared and red signals to the NDVI. The WDRVI is particularly effective in scenes that have moderate-to-high vegetation density when NDVI exceeds 0.6. NDVI tends to level off when vegetation fraction and leaf area index (LAI) increase, whereas the WDRVI is more sensitive to a wider range of vegetation fractions and to changes in LAI. The weighting coefficient (a) can range from 0.1 to 0.2. ENVI uses a value of 0.2, as recommended by Henebry, Viña, and Gitelson (2004) [152]	2004	[169]
Green Optimized Soil-Adjusted Vegetation Index	GOSAVI = (NIR-Green)/ (NIR + Green + 0.16)	North Carolina, USA	This index was originally designed with color–infrared photography to predict nitrogen requirements for corn. It is similar to OSAVI, but it substitutes the green band for red [152]	2005	[170]
Green Difference	GDVI = NIR - Green	North Carolina Coastal Plain, USA	Aerial photography used for nitrogen requirements in corn	2006	[171]
Green Ratio Vegetation Index	GRVI = NIR/Green	North Carolina Coastal Plain, USA	Aerial photography used for nitrogen requirements in corn	2006	[171]

Table A2. *Cont.*

Vegetation Indices (VIs)	Formulas	Study Area	Observations	Year	Ref.
Modified Nonlinear Index	MNLI = $((NIR^2 - Red) \times (1 + L))/(NIR^2 + Red + L)$	Colorado, USA	Multispectral satellite images. The impact of using band ratio and vegetation indices of the AWIFS sensor images to the crop classification accuracy is empirically investigated via supervised classification. The research indicates that appropriately used vegetation indices and image ratios can potentially improve crop classification accuracy	2008	[172]
MERIS terrestrial chlorophyll index	MTCI = (R740 − R705)/(R705 − R665)	Southampton, UK	This paper reports on the design and indirect evaluation of a surrogate REP index for use with spectral data recorded at the standard band settings of the Medium Resolution Imaging Spectrometer (MERIS). This index, termed the MERIS terrestrial chlorophyll index (MTCI), was evaluated using model spectra, field spectra, and MERIS data	2010	[173]
Normalized Area Over Reflectance Curve	$NAOC = 1 - \frac{\int_a^b \rho d\lambda}{\rho_{max}(b-a)}$ Where ρ is the reflectance; λ is the wavelength; ρmax is the maximum far-red reflectance, corresponding to reflectance at the wavelength "b"; and "a" and "b" are the integration limits surrounding the chlorophyll well centered at ∼670 nm.	Valencia, Spain	The Normalized Area Over Reflectance Curve (NAOC) is proposed as a new index for remote sensing estimation of the leaf chlorophyll content of heterogeneous areas with different crops, different canopies, and different types of bare soil. This index is based on the calculation of the area over the reflectance curve obtained by high spectral resolution reflectance measurements determined from the integral of the red–near-infrared interval and divided by the maximum reflectance in that spectral region	2010	[75]

Table A2. *Cont.*

Vegetation Indices (VIs)	Formulas	Study Area	Observations	Year	Ref.
Triangular Greenness Index	TGI = ((λRed − λBlue)(ρRed − ρGreen) − (λRed − λGreen)(ρRed − ρBlue))/2	Maryland, USA	This index approximates the area of a triangle bounding a leaf reflectance spectrum, where the vertices are in the red, green, and blue wavelengths. The Lambda (λ) terms represent the center wavelengths of the respective bands. The Rho (ρ) terms represent the pixel values of those bands. The original TGI equation (Hunt et al., 2011) used 670 nm, 550 nm, and 480 nm for the red, green, and blue wavelength centers, with a 10 nm band width [152]	2011	[174]
WorldView Improved Vegetative Index	WV-VI = (NIR^2-Red)/(NIR^2 + Red)	Maryland, USA	This index uses WorldView-2 bands to compute NDVI. The value of this index ranges from −1 to 1. The common range for green vegetation is 0.2 to 0.8 [152]	2012	[175]
Enhanced Normalized Difference Vegetation Index	ENDVI = ((NIR + Green) − (2 × Blue))/((NIR + Green) + (2 × Blue))	Carlstadt, USA	The blue channel for NDVI can be used equally as well for the visible absorption channel as the Kodak film using red as the visible absorption channel Maxar found that better results are achieved using red and green as the reflective channels while using blue as the absorption channel	2015	[176–179]

References

1. Furukawa, K. Resource Base: Global Distribution and Characteristics of Estuaries and Associated Coastal Shores. *Treatise Estuar. Coast. Sci.* **2012**, *1*, 207–228. [CrossRef]
2. Earthdata What Is Remote Sensing? 2022. Available online: https://www.earthdata.nasa.gov/learn/backgrounders/remote-sensing (accessed on 23 September 2022).
3. Horning, N. Remote Sensing. *Encycl. Ecol.* **2019**, *7*, 404–413. [CrossRef]
4. Xiong, X.; Butler, J. Volume 1 Overview. *Compr. Remote Sens.* **2018**, *1*, 1–6. [CrossRef]
5. Calvet, J.-C.; Albergel, C.; Baghdadi, N.; Leroux, D.; Munier, S. Chapter 6—Remote sensing. *Water Resour. Mediterr. Reg.* **2020**, *1*, 137–156. [CrossRef]
6. Haus, H.A.; Melcher, J.R. *Electromagnetic Fields and Energy*; Prentice Hall: Cambridge, MA, USA, 1989.
7. Lorrain, P. *Fundamentals of Electromagnetic Phenomena*; W.H. Freeman: New York, NY, USA, 2000.
8. Adler, R.B.; Chu, L.J.; Fano, R.M. *Electromagnetic Energy Transmission and Radiation*; The MIT Press: Cambridge, MA, USA, 1968.
9. Ting, D. Thermal radiation. *Thermofluids* **2022**, 357–372. [CrossRef]
10. Rani, M.; Masroor, M.; Kumar, P. Remote sensing of Ocean and Coastal Environment—Overview. *Remote Sens. Ocean Coast. Environ.* **2021**, *1*, 1–15. [CrossRef]
11. Krug, L.A.; Platt, T.; Sathyendranath, S.; Barbosa, A.B. Ocean surface partitioning strategies using ocean colour remote Sensing: A review. *Prog. Oceanogr.* **2017**, *155*, 41–53. [CrossRef]
12. Gale, M.G.; Cary, G.J.; Van Dijk, A.I.J.M.; Yebra, M. Forest fire fuel through the lens of remote sensing: Review of approaches, challenges and future directions in the remote sensing of biotic determinants of fire behaviour. *Remote Sens. Environ.* **2021**, *255*, 112282. [CrossRef]
13. Yu, Y.; Fu, L.; Cheng, Y.; Ye, Q. Multi-view distance metric learning via independent and shared feature subspace with applications to face and forest fire recognition, and remote sensing classification. *Knowledge-Based Syst.* **2022**, *243*, 108350. [CrossRef]
14. de Jesus, C.S.L.; Delgado, R.C.; Wanderley, H.S.; Teodoro, P.E.; Pereira, M.G.; Lima, M.; de Ávila Rodrigues, R.; da Silva Junior, C.A. Fire risk associated with landscape changes, climatic events and remote sensing in the Atlantic Forest using ARIMA model. *Remote Sens. Appl. Soc. Environ.* **2022**, *26*, 100761. [CrossRef]
15. Wetherley, E.B.; Roberts, D.A.; Tague, C.L.; Jones, C.; Quattrochi, D.A.; McFadden, J.P. Remote sensing and energy balance modeling of urban climate variability across a semi-arid megacity. *Urban Clim.* **2021**, *35*, 100757. [CrossRef]
16. Avand, M.; Moradi, H.; lasboyee, M.R. Using machine learning models, remote sensing, and GIS to investigate the effects of changing climates and land uses on flood probability. *J. Hydrol.* **2021**, *595*, 125663. [CrossRef]
17. Ganci, G.; Cappello, A.; Bilotta, G.; Del Negro, C. How the variety of satellite remote sensing data over volcanoes can assist hazard monitoring efforts: The 2011 eruption of Nabro volcano. *Remote Sens. Environ.* **2020**, *236*, 111426. [CrossRef]
18. McAlpin, D.; Meyer, F.J. Multi-sensor data fusion for remote sensing of post-eruptive deformation and depositional features at Redoubt Volcano. *J. Volcanol. Geotherm. Res.* **2013**, *259*, 414–423. [CrossRef]
19. Fu, X.; Yao, L.; Xu, W.; Wang, Y.; Sun, S. Exploring the multitemporal surface urban heat island effect and its driving relation in the Beijing-Tianjin-Hebei urban agglomeration. *Appl. Geogr.* **2022**, *144*, 102714. [CrossRef]
20. Bovolo, F.; Bruzzone, L.; Solano-Correa, Y.T. Multitemporal Analysis of Remotely Sensed Image Data. *Compr. Remote Sens.* **2018**, *2*, 156–185. [CrossRef]
21. Wu, X.; Xiao, Q.; Wen, J.; You, D.; Hueni, A. Advances in quantitative remote sensing product validation: Overview and current status. *Earth-Sci. Rev.* **2019**, *196*, 102875. [CrossRef]
22. Rivera-Marin, D.; Dash, J.; Ogutu, B. The use of remote sensing for desertification studies: A review. *J. Arid Environ.* **2022**, *206*, 104829. [CrossRef]
23. Veettil, B.K.; Hong Quan, N.; Hauser, L.T.; Doan Van, D.; Quang, N.X. Coastal and marine plastic litter monitoring using remote sensing: A review. *Estuar. Coast. Shelf Sci.* **2022**, *279*, 108160. [CrossRef]
24. Wang, P.; Bayram, B.; Sertel, E. A comprehensive review on deep learning based remote sensing image super-resolution methods. *Earth-Sci. Rev.* **2022**, *232*, 104110. [CrossRef]
25. Ali, A.M.; Abouelghar, M.; Belal, A.A.; Saleh, N.; Yones, M.; Selim, A.I.; Amin, M.E.S.; Elwesemy, A.; Kucher, D.E.; Maginan, S.; et al. Crop Yield Prediction Using Multi Sensors Remote Sensing (Review Article). *Egypt. J. Remote Sens. Space Sci.* **2022**, *25*, 711–716. [CrossRef]
26. Liu, C.; Xing, C.; Hu, Q.; Wang, S.; Zhao, S.; Gao, M. Stereoscopic hyperspectral remote sensing of the atmospheric environment: Innovation and prospects. *Earth-Sci. Rev.* **2022**, *226*, 103958. [CrossRef]
27. Chen, Z.; Deng, L.; Luo, Y.; Li, D.; Marcato Junior, J.; Nunes Gonçalves, W.; Awal Md Nurunnabi, A.; Li, J.; Wang, C.; Li, D. Road extraction in remote sensing data: A survey. *Int. J. Appl. Earth Obs. Geoinf.* **2022**, *112*, 102833. [CrossRef]
28. Shirmard, H.; Farahbakhsh, E.; Müller, R.D.; Chandra, R. A review of machine learning in processing remote sensing data for mineral exploration. *Remote Sens. Environ.* **2022**, *268*, 112750. [CrossRef]
29. Asadzadeh, S.; de Oliveira, W.J.; de Souza Filho, C.R. UAV-based remote sensing for the petroleum industry and environmental monitoring: State-of-the-art and perspectives. *J. Pet. Sci. Eng.* **2022**, *208*, 109633. [CrossRef]
30. Tommasini, M.; Bacciottini, A.; Gherardelli, M. A QGIS Tool for Automatically Identifying Asbestos Roofing. *ISPRS Int. J. Geo-Inf.* **2019**, *8*, 131. [CrossRef]

31. Stevulova, N.; Estokova, A.; Holub, M.; Singovszka, E. Demolition waste contaminated with asbestos. *Adv. Toxic. Constr. Build. Mater.* **2022**, *1*, 261–283. [CrossRef]
32. Obmiński, A. Asbestos cement products and their impact on soil contamination in relation to various sources of anthropogenic and natural asbestos pollution. *Sci. Total Environ.* **2022**, *848*, 157275. [CrossRef]
33. OMS. Eliminación de las Enfermedades Relacionadas con el Asbestos. 2020. Available online: https://www.who.int/es/news-room/fact-sheets/detail/asbestos-elimination-of-asbestos-related-diseases (accessed on 2 December 2022).
34. Frank, A.L.; Joshi, T.K. The global spread of asbestos. *Ann. Glob. Heal.* **2014**, *80*, 257–262. [CrossRef]
35. Villamizar, G.; Camero, G. *Asbesto en Colombia. Fundamentos Para el Debate*; Universidad Nacional de Colombia: Bogotá, Colombia, 2019.
36. Książek, J. Methods for Detection of Asbestos-Cement Roof ng Sheets. *Geomatics Environ. Eng.* **2014**, *8*, 59–76. [CrossRef]
37. Hemminki, K.; Försti, A.; Chen, T.; Hemminki, A. Incidence, mortality and survival in malignant pleural mesothelioma before and after asbestos in Denmark, Finland, Norway and Sweden. *BMC Cancer* **2021**, *21*, 1189. [CrossRef] [PubMed]
38. Statista. Major Countries in Worldwide Asbestos Mine Production in 2021. 2021. Available online: https://www.statista.com/statistics/264923/world-mine-production-of-asbestos/ (accessed on 7 October 2022).
39. Carmonaa, R.E.; Rivera Rosalesa, R.M. Asbestosis y mesotelioma pleural maligno. *Rev. Fac. Med.* **2013**, *52*, 5–17.
40. Selikoff, I.J.; Lee, D.H.K. Asbestos and disease. *Asbestos Dis.* **1979**, *36*, 157–158. [CrossRef]
41. Navarro-Vargas, J.R.; Villamizar, G.A. Artículo de Reflexión El largo y sinuoso camino de la enfermedad laboral en Colombia. El caso de la asbestosis. *Rev. De La Acad. Nac. De Med.* **2019**, 231–240.
42. Neitzel, R.L.; Sayler, S.K.; Demond, A.H.; d'Arcy, H.; Garabrant, D.H.; Franzblau, A. Measurement of asbestos emissions associated with demolition of abandoned residential dwellings. *Sci. Total Environ.* **2020**, *722*, 137891. [CrossRef] [PubMed]
43. Frassy, F.; Candiani, G.; Rusmini, M.; Maianti, P.; Marchesi, A.; Nodari, F.R.; Via, G.D.; Albonico, C.; Gianinetto, M. Mapping asbestos-cement roofing with hyperspectral remote sensing over a large mountain region of the Italian western alps. *Sensors* **2014**, *14*, 15900–15913. [CrossRef] [PubMed]
44. Krówczyńska, M.; Raczko, E.; Staniszewska, N.; Wilk, E. Asbestos-cement roofing identification using remote sensing and convolutional neural networks (CNNs). *Remote Sens.* **2020**, *12*, 408. [CrossRef]
45. Suomalainen, J.; Oliveira, R.A.; Hakala, T.; Koivumäki, N.; Markelin, L.; Näsi, R.; Honkavaara, E. Direct reflectance transformation methodology for drone-based hyperspectral imaging. *Remote Sens. Environ.* **2021**, *266*, 112691. [CrossRef]
46. Pfitzner, K.; Bartolo, R.; Whiteside, T.; Loewensteiner, D.; Esparon, A. Multi-temporal spectral reflectance of tropical savanna understorey species and implications for hyperspectral remote sensing. *Int. J. Appl. Earth Obs. Geoinf.* **2022**, *112*, 102870. [CrossRef]
47. Scopus. Scopus Research. 2020. Available online: https://unicartagena.elogim.com:2085/results/results.uri?sort=plf-f&src=s&st1=Asbestos+&nlo=&nlr=&nls=&sid=ab9cb7ceaa0a84c920417ae66c0e2036&sot=b&sdt=cl&cluster=scoaffilctry%2C%22Colombia%22%2Ct&sl=24&s=TITLE-ABS-KEY%28Asbestos+%29&cl=t&offset=21&origin=r (accessed on 7 October 2020).
48. Bedini, E. Application of WorldView-3 imagery and ASTER TIR data to map alteration minerals associated with the Rodalquilar gold deposits, southeast Spain. *Adv. Space Res.* **2019**, *63*, 3346–3357. [CrossRef]
49. Carlos Chicaíza-Rojas, L.; Francisco Lopez-Parra, J. Uso de imágenes satelitales para detección y cuantificación de asbesto. *DYNA* **2014**, *81*, 1–2.
50. The European Space Agency. WorldView-3 Instruments. 2022. Available online: https://earth.esa.int/eogateway/missions/worldview-3 (accessed on 13 December 2022).
51. Szabó, S.; Burai, P.; Kovács, Z.; Szabó, G.; Kerényi, A.; Fazekas, I.; Paládi, M.; Buday, T.; Szabó, G. Testing algorithms for the identification of asbestos roofing based on hyperspectral data. *Environ. Eng. Manag. J.* **2014**, *143*, 512900. [CrossRef]
52. Cilia, C.; Panigada, C.; Rossini, M.; Candiani, G.; Pepe, M.; Colombo, R. Mapping of Asbestos Cement Roofs and Their Weathering Status Using Hyperspectral Aerial Images. *ISPRS Int. J. Geo-Inf.* **2015**, *4*, 928–941. [CrossRef]
53. Gibril, M.B.A.; Shafri, H.Z.M.; Hamedianfar, A. New semi-automated mapping of asbestos cement roofs using rule-based object-based image analysis and Taguchi optimization technique from WorldView-2 images. *Int. J. Remote Sens.* **2017**, *38*, 467–491. [CrossRef]
54. Bassani, C.; Cavalli, R.M.; Cavalcante, F.; Cuomo, V.; Palombo, A.; Pascucci, S.; Pignatti, S. Deterioration status of asbestos-cement roofing sheets assessed by analyzing hyperspectral data. *Remote Sens. Environ.* **2007**, *109*, 361–378. [CrossRef]
55. Norman, M.; Mohd Shafri, H.Z.; Idrees, M.O.; Mansor, S.; Yusuf, B. Spatio-statistical optimization of image segmentation process for building footprint extraction using very high-resolution WorldView 3 satellite data. *Geocarto Int.* **2019**, *35*, 1124–1147. [CrossRef]
56. Abriha, D.; Kovács, Z.; Ninsawat, S.; Bertalan, L.; Balázs, B.; Szabó, S. Identification of roofing materials with Discriminant Function Analysis and Random Forest classifiers on pan-sharpened WorldView-2 imagery—A comparison. *Hungarian Geogr. Bull.* **2018**, *67*, 375–392. [CrossRef]
57. Fiumi, L.; Campopiano, A.; Casciardi, S.; Ramires, D. Method validation for the identification of asbestos–cement roofing. *Appl. Geomatics* **2012**, *4*, 55–64. [CrossRef]
58. Wu, P.-Y.; Sandels, C.; Mjörnell, K.; Mangold, M.; Johansson, T. Predicting the presence of hazardous materials in buildings using machine learning. *Build. Environ.* **2022**, *213*, 108894. [CrossRef]

59. Ashtari, A.; Alizadeh, B. A comparative study of machine learning classifiers for secure RF-PUF-based authentication in internet of things. *Microprocess. Microsyst.* **2022**, *93*, 104600. [CrossRef]
60. LeCun, Y.; Boser, B.; Denker, J.S.; Henderson, D.; Howard, R.E.; Hubbard, W.; Jackel, L.D. Backpropagation Applied to Handwritten Zip Code Recognition. *Neural Comput.* **1989**, *1*, 541–551. [CrossRef]
61. Krizhevsky, B.A.; Sutskever, I.; Hinton, G.E. ImageNet Classification with Deep Convolutional Neural Networks. *Commun. ACM* **2012**, *60*, 84–90. [CrossRef]
62. Kazan-Allen, L. *Asbestos Profile: European Union*; International Asbestos Ban Secretariat: Bruxelles, Belgium, 2019; Available online: http://www.ibasecretariat.org/prof_eu.php (accessed on 23 September 2022).
63. Norman, M.; Shafri, H.Z.M.; Mansor, S.; Yusuf, B.; Radzali, N.A.W.M. Fusion of multispectral imagery and LiDAR data for roofing materials and roofing surface conditions assessment. *Int. J. Remote Sens.* **2020**, *41*, 1–22. [CrossRef]
64. García-Pardo, K.A.; Moreno-Rangel, D.; Domínguez-Amarillo, S.; García-Chávez, J.R. Remote sensing for the assessment of ecosystem services provided by urban vegetation: A review of the methods applied. *Urban For. Urban Green.* **2022**, *74*, 127636. [CrossRef]
65. Neinavaz, E.; Schlerf, M.; Darvishzadeh, R.; Gerhards, M.; Skidmore, A.K. Thermal infrared remote sensing of vegetation: Current status and perspectives. *Int. J. Appl. Earth Obs. Geoinf.* **2021**, *102*, 102415. [CrossRef]
66. Pérez-Cabello, F.; Montorio, R.; Alves, D.B. Remote sensing techniques to assess post-fire vegetation recovery. *Curr. Opin. Environ. Sci. Heal.* **2021**, *21*, 100251. [CrossRef]
67. Andreatta, D.; Gianelle, D.; Scotton, M.; Dalponte, M. Estimating grassland vegetation cover with remote sensing: A comparison between Landsat-8, Sentinel-2 and PlanetScope imagery. *Ecol. Indic.* **2022**, *141*, 109102. [CrossRef]
68. Meusburger, K.; Bänninger, D.; Alewell, C. Estimating vegetation parameter for soil erosion assessment in an alpine catchment by means of QuickBird imagery. *Int. J. Appl. Earth Obs. Geoinf.* **2010**, *12*, 201–207. [CrossRef]
69. Henrich, V.; Krauss, G.; Götze, C.; Sandow, C. Index DataBase. A Database for Remote Sensing Indices. 2012. Available online: https://www.indexdatabase.de/db/i.php (accessed on 29 September 2022).
70. Huang, S.; Tang, L.; Hupy, J.P.; Wang, Y.; Shao, G. A commentary review on the use of normalized difference vegetation index (NDVI) in the era of popular remote sensing. *J. For. Res.* **2021**, *32*, 1–6. [CrossRef]
71. Beltrán Hernández, D.H. *Aplicación de Indices de Vegetación Para Evaluar Procesos de Restauración Ecológica en el Parque Forestal Embalse del Neusa*; Universidad Militar Nueva Granada: Neusa, Colombia, 2017.
72. Song, Y.; Chen, B.; Ho, H.C.; Kwan, M.-P.; Liu, D.; Wang, F.; Wang, J.; Cai, J.; Li, X.; Xu, Y.; et al. Observed inequality in urban greenspace exposure in China. *Environ. Int.* **2021**, *156*, 106778. [CrossRef]
73. Sánchez-Méndez, A.G.; Arguijo-Hernández, S.P. Análisis de imágenes multiespectrales para la detección de cultivos y detección de plagas y enfermedades en la producción de café. *Res. Comput. Sci.* **2018**, *147*, 309–317. [CrossRef]
74. Pedrali, L.D.; Borges Júnior, N.; Pereira, R.S.; Tramontina, J.; Alba, E.; Marchesan, J. Multispectral remote sensing for determining dry severity levels of pointers in *Eucalyptus* spp. *Sci. For.* **2019**, *122*, 224–234.
75. Vales, J.J.; Pino, I.; Granado, L.; Prieto, R.; Méndez, E.; Rodríguez, M.; Giménez de Azcárate, F.; Ortega, E.; Moreira, J.M. Cartografía de la afección y recuperación vegetal del incendio de Las Peñuelas en Moguer (Huelva) con imágenes satelitales. *Rev. Teledetección* **2020**, *57*, 79. [CrossRef]
76. Michalijos, M.P.; Uboldi, J. Propuesta metodológica para la evaluación de áreas afectadas por incendios mediante el uso de imágenes satelitales (Sierra de la Ventana, Argentina). *Rev. Geogr. Norte Gd.* **2013**, *56*, 223–234. [CrossRef]
77. Delegido, J.; Alonso, L.; González, G.; Moreno, J. Estimating chlorophyll content of crops from hyperspectral data using a normalized area over reflectance curve (NAOC). *Int. J. Appl. Earth Obs. Geoinf.* **2010**, *12*, 165–174. [CrossRef]
78. Saito, H.; Uchiyama, S.; Teshirogi, K. Rapid vegetation recovery at landslide scars detected by multitemporal high-resolution satellite imagery at Aso volcano, Japan. *Geomorphology* **2022**, *398*, 107989. [CrossRef]
79. Dennison, P.E.; Roberts, D.A. The effects of vegetation phenology on endmember selection and species mapping in southern California chaparral. *Remote Sens. Environ.* **2003**, *87*, 295–309. [CrossRef]
80. Dennison, P.E.; Roberts, D.A. Endmember selection for multiple endmember spectral mixture analysis using endmember average RMSE. *Remote Sens. Environ.* **2003**, *87*, 123–135. [CrossRef]
81. Kokaly, R.F.; Despain, D.G.; Clark, R.N.; Livo, K.E. Mapping vegetation in Yellowstone National Park using spectral feature analysis of AVIRIS data. *Remote Sens. Environ.* **2003**, *84*, 437–456. [CrossRef]
82. Frassy, F.; Maianti, P.; Marchesi, A.; Nodari, F.R.; Dalla Via, G.; De Paulis, R.; Biffi, P.G.; Gianinetto, M. Satellite remote sensing for hydrocarbon exploration in new venture areas. In Proceedings of the 2015 IEEE International Geoscience and Remote Sensing Symposium (IGARSS), Milan, Italy, 26–31 July 2015; pp. 2884–2887. [CrossRef]
83. Fingas, M.; Wang, Z.; Fieldhouse, B.; Smith, P. Environment Canada Arctic and Marine Oil Spill Program Technical Seminar (AMOP) Proceedings. 2003. Available online: https://www.researchgate.net/publication/256925779_The_correlation_of_chemical_characteristics_of_an_oil_to_dispersant_effectiveness (accessed on 2 December 2022).
84. Salisbury, J.W.; D'Aria, D.M.; Sabins, F.F. Thermal infrared remote sensing of crude oil slicks. *Remote Sens. Environ.* **1993**, *45*, 225–231. [CrossRef]
85. Sabins, F.F. Remote sensing for petroleum exploration, Part 1: Overview of imaging systems. *Lead. Edge* **2012**, *17*, 467. [CrossRef]
86. Desmond, D.S.; Crabeck, O.; Lemes, M.; Harasyn, M.L.; Mansoori, A.; Saltymakova, D.; Fuller, M.C.; Rysgaard, S.; Barber, D.G.; Isleifson, D.; et al. Investigation into the geometry and distribution of oil inclusions in sea ice using non-destructive X-ray

microtomography and its implications for remote sensing and mitigation potential. *Mar. Pollut. Bull.* **2021**, *173*, 112996. [CrossRef] [PubMed]
87. Aweda, E.D.; Adeyewa, Z.D. Inter annual variation of vegetation anomaly over Nigeria using satellite-derived index. *Adv. Appl. Sci. Res.* **2011**, *2*, 468–475.
88. Obida, C.B.; Blackburn, G.A.; Whyatt, J.D.; Semple, K.T. Counting the cost of the Niger Delta's largest oil spills: Satellite remote sensing reveals extensive environmental damage with >1million people in the impact zone. *Sci. Total Environ.* **2021**, *775*, 145854. [CrossRef]
89. Maianti, P.; Rusmini, M.; Tortini, R.; Dalla Via, G.; Frassy, F.; Marchesi, A.; Rota Nodari, F.; Gianinetto, M. Monitoring large oil slick dynamics with moderate resolution multispectral satellite data. *Nat. Hazards* **2014**, *73*, 473–492. [CrossRef]
90. Gianinetto, M.; Frassy, F.; Marchesi, A.; Maianti, P.; De Paulis, R.; Biffi, P.G.; Nodari, F.R. Mapping large-scale microseepage signals for supporting oil and gas exploration in new ventures. *Int. Geosci. Remote Sens. Symp.* **2016**, *2016*, 5430–5433. [CrossRef]
91. Bhadra, B.K.; Pathak, S.; Nanda, D.; Gupta, A.; Rao, S.S. Spectral characteristics of talc and mineral abundance mapping in the Jahazpur Belt of Rajasthan, India using AVIRIS-NG data. *Int. J. Remote Sens.* **2020**, *41*, 8757–8777. [CrossRef]
92. Camacho-Velasco, A.; Vargas-García, C.A.; Rojas-Morales, F.A.; Castillo-Castelblanco, S.F.; Arguello-Fuentes, H. Aplicaciones y retos del sensado remoto hiperespectral en la geología colombiana. *Rev. Fac. Ing.* **2015**, *24*, 17–29. [CrossRef]
93. Carrino, T.A.; Crósta, A.P.; Toledo, C.L.B.; Silva, A.M. Hyperspectral remote sensing applied to mineral exploration in southern Peru: A multiple data integration approach in the Chapi Chiara gold prospect. *Int. J. Appl. Earth Obs. Geoinf.* **2018**, *64*, 287–300. [CrossRef]
94. Thannoun, R.G. Mapping lithological and mineralogical units using hyperspectral imagery. *Malaysian J. Sci.* **2021**, *40*, 93–106. [CrossRef]
95. Fan, Y.; Wan, Y.; Wang, H.; Yang, X.; Liang, M.; Pan, C.; Zhang, S.; Wang, W.; Tan, F. Application of an airborne hyper-spectral survey system CASI/SASI in the gold-silver-lead-zinc ore district of Huaniushan, Gansu, China. *Geol. Croat.* **2021**, *74*, 73–83. [CrossRef]
96. Lyu, P.; He, L.; He, Z.; Liu, Y.; Deng, H.; Qu, R.; Wang, J.; Zhao, Y.; Wei, Y. Research on remote sensing prospecting technology based on multi-source data fusion in deep-cutting areas. *Ore Geol. Rev.* **2021**, *138*, 104359. [CrossRef]
97. Dkhala, B.; Mezned, N.; Gomez, C.; Abdeljaouad, S. Hyperspectral field spectroscopy and SENTINEL-2 Multispectral data for minerals with high pollution potential content estimation and mapping. *Sci. Total Environ.* **2020**, *740*, 140160. [CrossRef] [PubMed]
98. Peyghambari, S.; Zhang, Y. Hyperspectral remote sensing in lithological mapping, mineral exploration, and environmental geology: An updated review. *J. Appl. Remote. Sens.* **2021**, *15*, 031501. [CrossRef]
99. Coulter, D.W.; Harris, P.D.; Wickert, L.M.; Zhou, X. Advances in Spectral Geology and Remote Sensing: 2008–2017. In Proceedings of the Exploration 17: Sixth Decennial International Conference on Mineral Exploration, Toronto, ON, Canada, 21–25 October 2017; pp. 23–50.
100. Asadzadeh, S.; de Souza Filho, C.R. A review on spectral processing methods for geological remote sensing. *Int. J. Appl. Earth Obs. Geoinf.* **2016**, *47*, 69–90. [CrossRef]
101. Henrich., V.; Götze, C.; Jung, A.; Sandow, C.; Thürkow, D.; Glaesser, C. Development of an Online Indices Database: Motivation, Concept and Implementation | Request PDF. 2009. Available online: https://www.researchgate.net/publication/259802556_Development_of_an_online_indices_database_Motivation_concept_and_implementation (accessed on 29 September 2022).
102. Ukrainski, P. IDB: A Remote Sensing Indices Database. 2022. Available online: http://www.50northspatial.org/idb-remote-sensing-indices-database/ (accessed on 29 September 2022).
103. Zhang, X.; Pazner, M.; Duke, N. Lithologic and mineral information extraction for gold exploration using ASTER data in the south Chocolate Mountains (California). *ISPRS J. Photogramm. Remote Sens.* **2007**, *62*, 271–282. [CrossRef]
104. Kumar, C.; Chatterjee, S.; Oommen, T.; Guha, A. Automated lithological mapping by integrating spectral enhancement techniques and machine learning algorithms using AVIRIS-NG hyperspectral data in Gold-bearing granite-greenstone rocks in Hutti, India. *Int. J. Appl. Earth Obs. Geoinf.* **2020**, *86*, 102006. [CrossRef]
105. Amici, S.; Piscini, A.; Buongiorno, M.F.; Pieri, D. Geological classification of Volcano Teide by hyperspectral and multispectral satellite data. *Int. J. Remote Sens.* **2013**, *34*, 3356–3375. [CrossRef]
106. Bachri, I.; Hakdaoui, M.; Raji, M.; Teodoro, A.C.; Benbouziane, A. Machine Learning Algorithms for Automatic Lithological Mapping Using Remote Sensing Data: A Case Study from Souk Arbaa Sahel, Sidi Ifni Inlier, Western Anti-Atlas, Morocco. *ISPRS Int. J. Geo-Inf.* **2019**, *8*, 248. [CrossRef]
107. Caruso, A.S.; Clarke, K.D.; Tiddy, C.J.; Lewis, M.M. Airborne hyperspectral characterisation of hydrothermal alteration in a regolith-dominated terrain, southern Gawler Ranges, South Australia. *Aust. J. Earth Sci.* **2020**, *68*, 590–608. [CrossRef]
108. Sandoval, P.J.M.; González, J.A.C. *Principios y Aplicaciones de la Percepción Remota en el Cultivo de la Caña de Azúcar en Colombia*; Centro de investigación de la >caña de azúcar de Colombia: Cali, Colombia, 2012.
109. Negi, H.S.; Shekhar, C.; Singh, S.K. Snow and glacier investigations using hyperspectral data in the Himalaya. *Curr. Sci.* **2015**, *108*, 892–902.
110. Kokaly, R.F.; Clark, R.N.; Swayze, G.A.; Livo, K.E.; Hoefen, T.M.; Pearson, N.C.; Wise, R.A.; Benzel, W.M.; Lowers, H.A.; Driscoll, R.L.; et al. *USGS Spectral Library Version 7: U.S. Geological Survey Data Series 1035*; U.S. Geological Survey: Reston, VA, USA, 2017.

111. Bonifazi, G.; Capobianco, G.; Serranti, S. Asbestos containing materials detection and classification by the use of hyperspectral imaging. *J. Hazard. Mater.* **2018**, *344*, 981–993. [CrossRef] [PubMed]
112. Samsudin, S.H.; Shafri, H.Z.M.; Hamedianfar, A. Development of spectral indices for roofing material condition status detection using field spectroscopy and WorldView-3 data. *J. Appl. Remote Sens.* **2016**, *10*, 025021. [CrossRef]
113. Kokaly, R.F.; Couvillion, B.R.; Holloway, J.A.M.; Roberts, D.A.; Ustin, S.L.; Peterson, S.H.; Khanna, S.; Piazza, S.C. Spectroscopic remote sensing of the distribution and persistence of oil from the Deepwater Horizon spill in Barataria Bay marshes. *Remote Sens. Environ.* **2013**, *129*, 210–230. [CrossRef]
114. Clark, R.N.; Swayze, G.A.; Leifer, I.; Livo, K.E.; Lundeen, S.; Eastwood, M.; Green, R.O.; Kokaly, R.F.; Hoefen, T.; Sarture, C.; et al. A Method for Qualitative Mapping of Thick Oil Spills Using Imaging Spectroscopy. *U.S. Geol. Surv.* **2010**, *2010*, 51.
115. De Jong, S.M. Chapter 1 Basics of Remote Sensing. In *Remote Sensing Image Analysis: Including the Spatial Domain*; Springer: Dordrecht, The Netherlands, 2007; pp. 1–15. [CrossRef]
116. Liu, J.; Fan, J.; Yang, C.; Xu, F.; Zhang, X. Novel vegetation indices for estimating photosynthetic and non-photosynthetic fractional vegetation cover from Sentinel data. *Int. J. Appl. Earth Obs. Geoinf.* **2022**, *109*, 102793. [CrossRef]
117. Ma, X.Q.; Leng, P.; Liao, Q.Y.; Geng, Y.J.; Zhang, X.; Shang, G.F.; Song, X.; Song, Q.; Li, Z.L. Prediction of vegetation phenology with atmospheric reanalysis over semiarid grasslands in Inner Mongolia. *Sci. Total Environ.* **2022**, *812*, 152462. [CrossRef]
118. Bai, Y.; Li, S.; Liu, M.; Guo, Q. Assessment of vegetation change on the Mongolian Plateau over three decades using different remote sensing products. *J. Environ. Manag.* **2022**, *317*, 115509. [CrossRef]
119. Sun, W.; Liu, S.; Zhang, X.; Zhu, H. Performance of hyperspectral data in predicting and mapping zinc concentration in soil. *Sci. Total Environ.* **2022**, *824*, 153766. [CrossRef]
120. Ge, X.; Ding, J.; Teng, D.; Xie, B.; Zhang, X.; Wang, J.; Han, L.; Bao, Q.; Wang, J. Exploring the capability of Gaofen-5 hyperspectral data for assessing soil salinity risks. *Int. J. Appl. Earth Obs. Geoinf.* **2022**, *112*, 102969. [CrossRef]
121. Zambrano Prado P., L. Assessing Building's Rooftops Potencial to Integrate Food, Water and Energy Sysitems: The Use of Remote Sensing Technology and Percemptual Aspects in a Mediterranean Region. Universitat Autonoma de Barcelona. 2021. Available online: https://www.tdx.cat/bitstream/10803/674530/1/plzp1de1.pdf (accessed on 2 September 2022).
122. Kit, O.; Lüdeke, M.; Reckien, D. Texture-based identification of urban slums in Hyderabad, India using remote sensing data. *Appl. Geogr.* **2012**, *32*, 660–667. [CrossRef]
123. Nadal, A.; Alamús, R.; Pipia, L.; Ruiz, A.; Corbera, J.; Cuerva, E.; Rieradevall, J.; Josa, A. Urban planning and agriculture. Methodology for assessing rooftop greenhouse potential of non-residential areas using airborne sensors. *Sci. Total Environ.* **2017**, *601*, 493–507. [CrossRef] [PubMed]
124. Zini, E. Esperienze ed Esigenze di ARPA Lombardia di Utilizzazione del Telerilevamento Iperspettrale nei Monitoraggi e nei Controlli Ambientali; San Piero a Grado (Pisa). 2018. Available online: http://conferenzecisam.it/convegni/c-i-s-a-m-2018-1/documenti/Zini_ARPALombardia.pdf (accessed on 28 November 2022).
125. Lorenz, C.; Chiaravalloti-Neto, F.; de Oliveira Lage, M.; Quintanilha, J.A.; Parra, M.C.; Dibo, M.R.; Fávaro, E.A.; Guirado, M.M.; Nogueira, M.L. Remote sensing for risk mapping of Aedes aegypti infestations: Is this a practical task? *Acta Trop.* **2020**, *205*, 105398. [CrossRef] [PubMed]
126. Raczko, E.; Krówczyńska, M.; Wilk, E. Asbestos roofing recognition by use of convolutional neural networks and high-resolution aerial imagery. Testing different scenarios. *Build. Environ.* **2022**, *217*, 109092. [CrossRef]
127. Zhang, Y.L.; Hong, W.H.; Kim, Y.C. Methods for assessing asbestos-containing roofing slate distribution in an area with poor dwelling conditions. *J. Clean. Prod.* **2022**, *358*, 132032. [CrossRef]
128. Sobral, B.S.; de Oliveira-Júnior, J.F.; Alecrim, F.; Gois, G.; Muniz-Júnior, J.G.; de Bodas Terassi, P.M.; Pereira-Júnior, E.R.; Lyra, G.B.; Zeri, M. PERSIANN-CDR based characterization and trend analysis of annual rainfall in Rio De Janeiro State, Brazil. *Atmos. Res.* **2020**, *238*, 104873. [CrossRef]
129. Lammoglia, T.; de Souza Filho, C.R. Mapping and characterization of the API gravity of offshore hydrocarbon seepages using multispectral ASTER data. *Remote Sens. Environ.* **2012**, *123*, 381–389. [CrossRef]
130. Emran, B.J.; Tannant, D.D.; Najjaran, H. Low-altitude aerial methane concentration mapping. *Remote Sens.* **2017**, *9*, 823. [CrossRef]
131. Garcia-Pineda, O.; Staples, G.; Jones, C.E.; Hu, C.; Holt, B.; Kourafalou, V.; Graettinger, G.; DiPinto, L.; Ramirez, E.; Streett, D.; et al. Classification of oil spill by thicknesses using multiple remote sensors. *Remote Sens. Environ.* **2020**, *236*, 111421. [CrossRef]
132. Iwaszenko, S.; Kalisz, P.; Słota, M.; Rudzki, A. Detection of natural gas leakages using a laser-based methane sensor and uav. *Remote Sens.* **2021**, *13*, 510. [CrossRef]
133. Löw, F.; Stieglitz, K.; Diemar, O. Terrestrial oil spill mapping using satellite earth observation and machine learning: A case study in South Sudan. *J. Environ. Manag.* **2021**, *298*, 113424. [CrossRef] [PubMed]
134. Huang, X.; Zhang, B.; Perrie, W.; Lu, Y.; Wang, C. A novel deep learning method for marine oil spill detection from satellite synthetic aperture radar imagery. *Mar. Pollut. Bull.* **2022**, *179*, 113666. [CrossRef]
135. El-Hadidy, S.M.; Alshehri, F.; Sahour, H.; Abdelmalik, K.W. Detecting hydrocarbon micro-seepage and related contamination, probable prospect areas, deduced from a comparative analysis of multispectral and hyperspectral satellite images. *J. King Saud Univ.-Sci.* **2022**, *34*, 102192. [CrossRef]
136. Zoheir, B.; Emam, A. Integrating geologic and satellite imagery data for high-resolution mapping and gold exploration targets in the South Eastern Desert, Egypt. *J. Afr. Earth Sci.* **2012**, *66*, 22–34. [CrossRef]

137. Ghulam, A.; Amer, R.; Kusky, T.M. Mineral exploration and alteration zone mapping in eastern desert of Egypt using aster data. In Proceedings of the ASPRS 2010 Annual Conference, San Diego, CA, USA, 26–30 April 2010.
138. Lamri, T.; Djemaï, S.; Hamoudi, M.; Zoheir, B.; Bendaoud, A.; Ouzegane, K.; Amara, M. Satellite imagery and airborne geophysics for geologic mapping of the Edembo area, Eastern Hoggar (Algerian Sahara). *J. Afr. Earth Sci.* **2016**, *115*, 143–158. [CrossRef]
139. Epuh, E.E.; Okolie, C.J.; Daramola, O.E.; Ogunlade, F.S.; Oyatayo, F.J.; Akinnusi, S.A.; Emmanuel, E.O.I. An integrated lineament extraction from satellite imagery and gravity anomaly maps for groundwater exploration in the Gongola Basin. *Remote Sens. Appl. Soc. Environ.* **2020**, *20*, 100346. [CrossRef]
140. Eldosouky, A.M.; El-Qassas, R.A.Y.; Pour, A.B.; Mohamed, H.; Sekandari, M. Integration of ASTER satellite imagery and 3D inversion of aeromagnetic data for deep mineral exploration. *Adv. Space Res.* **2021**, *68*, 3641–3662. [CrossRef]
141. Muavhi, N.; Tessema, A. Identification of potential targets for kimberlite exploration using satellite imagery and map combination approach in the Lesotho Kimberlite Province. *Ore Geol. Rev.* **2021**, *132*, 104001. [CrossRef]
142. Soydan, H.; Koz, A.; Düzgün, H.Ş. Secondary Iron Mineral Detection via Hyperspectral Unmixing Analysis with Sentinel-2 Imagery. *Int. J. Appl. Earth Obs. Geoinf.* **2021**, *101*, 102343. [CrossRef]
143. Zouaghi, T.; Harbi, H. Airborne geophysics and remote sensing of an Nimas-Khadra area, southern Arabian shield: New insights into structural framework and mineral occurrences. *Adv. Space Res.* **2022**, *70*, 3649–3673. [CrossRef]
144. Jaud, M.; Geoffroy, L.; Chauvet, F.; Durand, E.; Civet, F. Potential of a virtual reality environment based on very-high-resolution satellite imagery for structural geology measurements of lava flows. *J. Struct. Geol.* **2022**, *158*, 104569. [CrossRef]
145. Epuh, E.E.; Moshood, A.I.; Okolie, C.J.; Daramola, O.E.; Akinnusi, S.A.; Arungwa, I.D.; Orji, M.J.; Olanrewaju, H.O.; Fatoyinbo, A.A. Integration of satellite gravimetry, multispectral imagery and digital elevation model for investigating crustal deformation in the Niger Delta Basin. *Geosyst. Geoenviron.* **2022**, *1*, 100067. [CrossRef]
146. Tözün, K.A.; Özyavaş, A. Automatic detection of geological lineaments in central Turkey based on test image analysis using satellite data. *Adv. Space Res.* **2022**, *69*, 3283–3300. [CrossRef]
147. Birth, G.S.; McVey, G.R. Measuring the Color of Growing Turf with a Reflectance Spectrophotometer. *Agron. J.* **1968**, *60*, 640–643. [CrossRef]
148. Rouse, J.W.J.; Haas, R.H.; Schell, J.A.; Deering, D.W.; Haas, R.H.; Schell, J.A.; Deering, D.W. Monitoring vegetation systems in the great plains with erts. Conference Paper, NASA. In Proceedings of the Goddard Space Flight Center 3d ERTS-1 Symp, Houston, TX, USA, 1974.
149. Kauth, R.J.; Thomas, G.S.P. *The Tasselled Cap—A Graphic Description of the Spectral-Temporal Development of Agricultural Crops as Seen by Landsat*; Pordue University: West Lafayette, IN, USA, 1976.
150. Tucker, C.J. Red and photographic infrared linear combinations for monitoring vegetation. *Remote Sens. Environ.* **1979**, *8*, 127–150. [CrossRef]
151. Huete, A.R. A soil-adjusted vegetation index (SAVI). *Remote Sens. Environ.* **1988**, *25*, 295–309. [CrossRef]
152. Crippen, R.E. Calculating the vegetation index faster. *Remote Sens. Environ.* **1990**, *34*, 71–73. [CrossRef]
153. Pinty, B.; Verstraete, M.M. GEMI: A non-linear index to monitor global vegetation from satellites. *Vegetatio* **1992**, *101*, 15–20. [CrossRef]
154. Kaufman, Y.J.; Tanre, D. Atmospherically resistant vegetation index (ARVI) for EOS-MODIS. *IEEE Trans. Geosci. Remote Sens.* **1992**, *30*, 261–270. [CrossRef]
155. L3Harris. Broadband Greenness. 2022. Available online: https://www.l3harrisgeospatial.com/docs/broadbandgreenness.html#:~{}:text=State%20University%2C%202005.-,Green%20Vegetation%20Index%20(GVI),range%20from%20-1%20to%201 (accessed on 27 September 2022).
156. Qi, J.; Chehbouni, A.; Huete, A.R.; Kerr, Y.H.; Sorooshian, S. A modified soil adjusted vegetation index. *Remote Sens. Environ.* **1994**, *48*, 119–126. [CrossRef]
157. Goel, N.S.; Qin, W. Influences of canopy architecture on relationships between various vegetation indices and LAI and Fpar: A computer simulation. *Remote Sens. Rev.* **1994**, *10*, 309–347. [CrossRef]
158. Roujean, J.L.; Breon, F.M. Estimating PAR absorbed by vegetation from bidirectional reflectance measurements. *Remote Sens. Environ.* **1995**, *51*, 375–384. [CrossRef]
159. Penuelas, J.; Baret, F.; Filella, I. Semi-empirical indices to assess carotenoids/chlorophyll a ratio from leaf spectral reflectance. *Photosynthetica* **1995**, *31*, 221–230.
160. Rondeaux, G.; Steven, M.; Baret, F. Optimization of soil-adjusted vegetation indices. *Remote Sens. Environ.* **1996**, *55*, 95–107. [CrossRef]
161. Gitelson, A.A.; Kaufman, Y.J.; Merzlyak, M.N. Use of a green channel in remote sensing of global vegetation from EOS-MODIS. *Remote Sens. Environ.* **1996**, *58*, 289–298. [CrossRef]
162. Chen, J.M. Evaluation of Vegetation Indices and a Modified Simple Ratio for Boreal Applications. *Can. J. Remote Sens.* **1996**, *22*, 229–242. [CrossRef]
163. Gitelson, A.A.; Merzlyak, M.N. Remote sensing of chlorophyll concentration in higher plant leaves. *Adv. Space Res.* **1998**, *22*, 689–692. [CrossRef]
164. Louhaichi, M.; Borman, M.M.; Johnson, D.E. Spatially Located Platform and Aerial Photography for Documentation of Grazing Impacts on Wheat. *Geocarto Int.* **2001**, *16*, 65–70. [CrossRef]
165. Minnett, P.J. Satellite Remote Sensing of Sea Surface Temperatures. *Encycl. Ocean Sci. Second Ed.* **2001**, *1*, 91–102. [CrossRef]

166. Huete, A.; Didan, K.; Miura, T.; Rodriguez, E.P.; Gao, X.; Ferreira, L.G. Overview of the radiometric and biophysical performance of the MODIS vegetation indices. *Remote Sens. Environ.* **2002**, *83*, 195–213. [CrossRef]
167. Boegh, E.; Soegaard, H.; Broge, N.; Schelde, K.; Thomsen, A.; Hasager, C.B.; Jensen, N.O. Airborne multispectral data for quantifying leaf area index, nitrogen concentration, and photosynthetic efficiency in agriculture. *Remote Sens. Environ.* **2002**, *81*, 179–193. [CrossRef]
168. Gitelson, A.A.; Stark, R.; Grits, U.; Rundquist, D.; Kaufman, Y.; Derry, D. Vegetation and soil lines in visible spectral space: A concept and technique for remote estimation of vegetation fraction. *Int. J. Remote Sens.* **2002**, *23*, 2537–2562. [CrossRef]
169. Bannari, A.; Asalhi, H.; Teillet, P.M. Transformed difference vegetation index (TDVI) for vegetation cover mapping. *IEEE Int. Geosci. Remote Sens. Symp.* **2002**, *5*, 3053–3055.
170. Gitelson, A.A.; Gritz, Y.; Merzlyak, M.N. Relationships between leaf chlorophyll content and spectral reflectance and algorithms for non-destructive chlorophyll assessment in higher plant leaves. *J. Plant Physiol.* **2003**, *160*, 271–282. [CrossRef]
171. Lobell, D.B.; Asner, G.P. Hyperion studies of crop stress in Mexico. In Proceedings of the 12th JPL Airborne Earth Science Workshop, Pasadena, CA, USA, 12–16 January 2004; pp. 1–6.
172. Gitelson, A.A. Wide Dynamic Range Vegetation Index for Remote Quantification of Biophysical Characteristics of Vegetation. *J. Plant Physiol.* **2004**, *161*, 165–173. [CrossRef]
173. Sripada, R.P. *Determining In-Season Nitrogen Requirements for Corn Using Aerial Color-Infrared Photography*; North Carolina State University: Raleigh, NC, USA, 2005.
174. Sripada, R.P.; Heiniger, R.W.; White, J.G.; Meijer, A.D. Aerial Color Infrared Photography for Determining Early In-Season Nitrogen Requirements in Corn. *Agron. J.* **2006**, *98*, 968–977. [CrossRef]
175. Yang, Z.; Willis, P.; Mueller, R. Impact of Band-Ratio Enhanced AWiFS Image to Crop Classification Accuracy. *Proc. Pecora.* **2008**, *17*, 1–11.
176. Dash, J.; Curran, P.J. The MERIS terrestrial chlorophyll index. *Int. J. Remote Sens.* **2004**, *25*, 5403–5413. [CrossRef]
177. Raymond Hunt, E.; Daughtry, C.S.T.; Eitel, J.U.H.; Long, D.S. Remote Sensing Leaf Chlorophyll Content Using a Visible Band Index. *Agron. J.* **2011**, *103*, 1090–1099. [CrossRef]
178. Wolf, A.F. Using WorldView-2 Vis-NIR multispectral imagery to support land mapping and feature extraction using normalized difference index ratios. In Proceedings of the Algorithms and Technologies for Multispectral, Hyperspectral, and Ultraspectral Imagery XVIII, Baltimore, MD, USA, 14 May 2012; Society of Photo-Optical Instrumentation Engineers (SPIE): Bellingham, DC, USA; Volume 8390, pp. 188–195. [CrossRef]
179. MaxMax. Enhanced Normalized Difference Vegetation Index (ENDVI). 2015. Available online: https://www.maxmax.com/endvi.htm (accessed on 26 September 2022).